CHALMERS
UNIVERSITY OF TECHNOLOGY

Resolved CO(1-0) Emission and Gas Properties in Luminous Dusty Star-forming Galaxies at z = 2-4

Citation for the original published paper (version of record):
Stanley, F., Jones, B., Riechers, D. et al (2023). Resolved CO(1-0) Emission and Gas Properties in Luminous Dusty Star-forming Galaxies at z = 2-4. Astrophysical Journal, 945(1).
http://dx.doi.org/10.3847/1538-4357/acb6f7

The Astrophysical Journal, 945:24 (19pp), 2023 March 1 https://doi.org/10.3847/1538-4357/acb6f7

Resolved CO(1–0) Emission and Gas Properties in Luminous Dusty Star-forming Galaxies at $z = 2–4$

F. Stanley[1,2], B. M. Jones[3,4], D. A. Riechers[3], C. Yang[5], S. Berta[2], P. Cox[1], T. J. L. C. Bakx[6,7], A. Cooray[8], H. Dannerbauer[9,10], S. Dye[11], D. H. Hughes[12], R. J. Ivison[13], S. Jin[14,15], M. Lehnert[16], R. Neri[2], A. Omont[1], P. van der Werf[17], and A. Weiss[18]

[1] Sorbonne Université, UPMC Université Paris 6 and CNRS, UMR 7095, Institut d'Astrophysique de Paris, 98b Boulevard Arago, F-75014 Paris, France
stanley@iram.fr
[2] Institut de Radioastronomie Millimétrique (IRAM), 300 Rue de la Piscine, F-38400 Saint-Martin-d'Hères, France
[3] I. Physikalisches Institut, Universität zu Köln, Zülpicher Strasse 77, D-50937 Köln, Germany
[4] Jodrell Bank Centre for Astrophysics, Department of Physics and Astronomy, School of Natural Sciences, The University of Manchester, Manchester, M13 9PL, UK
[5] Department of Space, Earth and Environment, Chalmers University of Technology, Onsala Space Observatory, SE-439 92 Onsala, Sweden
[6] Division of Particle and Astrophysical Science, Graduate School of Science, Nagoya University, Aichi 464-8602, Japan
[7] National Astronomical Observatory of Japan, 2-21-1, Osawa, Mitaka, Tokyo 181-8588, Japan
[8] Department of Physics and Astronomy, University of California, Irvine, CA92697, USA
[9] Instituto de Astrofísica de Canarias (IAC), E-38205 La Laguna, Tenerife, Spain
[10] Universidad de La Laguna, Departamento Astrofísica, E-38206 La Laguna, Tenerife, Spain
[11] School of Physics and Astronomy, University of Nottingham, University Park, Nottingham, NG7 2RD, UK
[12] Instituto Nacional de Astrofísica, Óptica y Electrónica, Luis Enrique Erro 1, Santa María Tonantzintla, Puebla 72840, Mexico
[13] European Southern Observatory, Karl-Schwarzschild-Strasse 2, D-85748 Garching, Germany
[14] Cosmic Dawn Center (DAWN), Copenhagen, Denmark
[15] DTU Space, Technical University of Denmark, Elektrovej 327, DK-2800 Kgs. Lyngby, Denmark
[16] Centre de Recherche Astrophysique de Lyon—CRAL, CNRS UMR 5574, UCBL1, ENSLyon, 9 avenue Charles André, F-69230 Saint-Genis-Laval, France
[17] Leiden Observatory, Leiden University, P.O. Box 9513, 2300 RA Leiden, The Netherlands
[18] Max-Planck-Institut für Radioastronomie, Auf dem Hügel 69, D-53121 Bonn, Germany

Received 2022 November 7; revised 2023 January 12; accepted 2023 January 27; published 2023 March 2

Abstract

We present the results of a survey of CO(1−0) emission in 14 infrared luminous dusty star-forming galaxies (DSFGs) at $2 < z < 4$ with the NSF's Karl G. Jansky Very Large Array. All sources are detected in ^{12}CO(1−0), with an angular resolution of $\sim 1''$. Seven sources show extended and complex structure. We measure CO luminosities of $(\mu)L'_{\rm CO(1-0)} = 0.4–2.9 \times 10^{11}$ K km s^{-1} pc^2, and molecular gas masses of $(\mu)M_{\rm H_2} = 1.3–8.6 \times 10^{11}\ M_\odot$, where (μ) is the magnification factor. The derived molecular gas depletion times of $t_{\rm dep} = 40–460$ Myr, cover the expected range of both normal star-forming galaxies and starbursts. Compared to the higher $-J$ CO transitions previously observed for the same sources, we find CO temperature brightness ratios of $r_{32/10} = 0.4–1.4$, $r_{43/10} = 0.4–1.7$, and $r_{54/10} = 0.3–1.3$. We find a wide range of CO spectral line energy distributions (SLEDs), in agreement with other high-z DSFGs, with the exception of three sources that are most comparable to Cloverleaf and APM08279+5255. Based on radiative transfer modeling of the CO SLEDs we determine densities of $n_{\rm H_2} = 0.3 - 8.5 \times 10^3$ cm^{-3} and temperatures of $T_{\rm K} = 100–200$ K. Lastly, four sources are detected in the continuum, three have radio emission consistent with their infrared-derived star formation rates, while HerBS-70E requires an additional synchrotron radiation component from an active galactic nucleus. Overall, we find that even though the sample is similarly luminous in the infrared, by tracing the CO(1−0) emission a diversity of galaxy and excitation properties are revealed, demonstrating the importance of CO(1−0) observations in combination to higher-J transitions.

Unified Astronomy Thesaurus concepts: High-redshift galaxies (734); Galaxies (573); Starburst galaxies (1570); CO line emission (262)

1. Introduction

Dusty star-forming galaxies (DSFGs) have played an important role in galaxy growth at high-z, as they dominate the cosmic star formation rate density (SFRD) up to redshifts of $z \sim 4$ (e.g., Magnelli et al. 2013; Bouwens et al. 2016, 2020; Bourne et al. 2017; Hatsukade et al. 2018; Zavala et al. 2021), including the peak of the SFRD at $z = 1–3$ (see Madau & Dickinson 2014). The most luminous DSFGs in the infrared (IR) can have luminosities at rest frame 8–1000 μm of $L_{\rm IR} > 10^{12}–10^{13}\ L_\odot$, corresponding to some of the most intense episodes of star formation activity, with star formation rates (SFRs) that can exceed 1000 $M_\odot$ yr^{-1} (see reviews by Blain et al. 2002; Casey et al. 2014; Hodge & da Cunha 2020).

The number of detected DSFGs at high-z has been steadily increasing over the last decades, with the advent of large area surveys, including the all-sky Planck-HFI (Cañameras et al. 2015; Planck Collaboration et al. 2015), and the South Pole Telescope (SPT; Carlstrom et al. 2011) surveys (Vieira et al. 2010, 2013), among others. The large field surveys on the Herschel Space Observatory (Herschel; Pilbratt et al. 2010) covering >1000 deg^2 of the extragalactic sky at 70–500 μm, have significantly contributed to the increased number of known DSFGs. Surveys such as the Herschel Astrophysical Terahertz Large Area Survey

(H-ATLAS; Eales et al. 2010), the Herschel Multi-tiered Extragalactic Survey (HerMES; Oliver et al. 2012), and the Herschel Stripe 82 Survey (HerS; Viero et al. 2014), have led to the detection of $>10^5$ DSFGs, including >200 luminous DSFGs with $S_{500\,\mu\mathrm{m}} = 80$–900 mJy (e.g., Nayyeri et al. 2016; Bakx et al. 2018, and references therein).

Dedicated follow-up studies of the luminous DSFGs identified with Herschel have found that these sources cover a wide redshift range of $1 < z < 6$ (e.g., Nayyeri et al. 2016; Bakx et al. 2018, and references therein), include numerous gravitationally amplified galaxies (e.g., Negrello et al. 2010, 2017; Conley et al. 2011; Cox et al. 2011; Riechers et al. 2011c; Bussmann et al. 2013; Wardlow et al. 2013; Nayyeri et al. 2016; Bakx et al. 2020a, 2020b), rare galaxies with $L_{\mathrm{IR}} > 10^{13}\,L_{\odot}$ classified as hyperluminous infrared galaxies (e.g., Fu et al. 2013; Ivison et al. 2013, 2019; Oteo et al. 2016; Riechers et al. 2013, 2017), and overdensities of DSFGs that are blended due to the large Herschel beam (e.g., Bussmann et al. 2015; Oteo et al. 2018; Gómez-Guijarro et al. 2019; Ivison et al. 2019). The diversity and size of the Herschel-selected DSFG population make it ideal for dedicated follow-up surveys of large statistical samples to determine the galaxy properties and nature of bright DSFGs at high-z.

Tracing the molecular gas in the interstellar medium of these galaxies is of particular interest, as it is the fuel for star formation. Direct observations of the ^{12}CO(1−0) transition are necessary to measure total molecular gas masses, and depletion timescales, probe the cold gas distribution and morphology, and anchor the modeling of the ^{12}CO spectral line energy distributions (SLEDs) from which the physical properties of the cold gas (e.g., kinetic temperature, and density) can be derived (e.g., Ivison et al. 2011; Riechers et al. 2011a, 2011c, 2011d; Harris et al. 2012; Aravena et al. 2016; Sharon et al. 2016).

A first necessary step toward this direction is the robust determination of the redshifts of these sources. Ongoing efforts have led to the measurement of spectroscopic redshifts for over ∼300 of the brightest high-z DSFGs (e.g., Weiß et al. 2009, 2013; Harris et al. 2012; Lupu et al. 2012; Walter et al. 2012; Strandet et al. 2016; Danielson et al. 2017; Fudamoto et al. 2017; Reuter et al. 2020; Urquhart et al. 2022), with z-GAL (Neri et al. 2020, P. Cox et al. 2023, in preparation) being the largest redshift survey among them.

The first series of z-GAL sources for which reliable spectroscopic redshifts were determined, was presented in Neri et al. (2020). In total 14 individual high-z luminous DSFGs were detected with NOEMA in 11 target fields that were Herschel selected based on their 500 μm fluxes. The sources were detected either in multiple ^{12}CO lines or in a combination of ^{12}CO and other molecular or atomic species. However, despite the multi-line detections, the conclusions of this study on the molecular gas properties of the sample remained limited due to the lack of information on the lowest-J ^{12}CO lines. This motivated targeted ^{12}CO(1−0) follow-up of these galaxies with the NSF's Karl G. Jansky Very Large Array (VLA).

In this paper, we present the survey of ^{12}CO(1−0) emission and the underlying radio continuum of 14 luminous DSFGs from the z-GAL Pilot Program in the redshift range of $2 < z < 4$. In Section 2, we describe the sample, the observations, and the data reduction. In Section 3, we report the main results from the VLA observations both for the ^{12}CO(1−0) emission line and the continuum. Section 4 outlines the implications of these results, particularly, addressing the total molecular gas mass, the excitation conditions, and the nature of these sources. Finally, Section 5 summarizes the main findings of this paper. Throughout this paper, we adopt a spatially flat Lambda cold dark matter cosmology with $H_0 = 67.4\ \mathrm{km\,s^{-1}\,Mpc^{-1}}$ and $\Omega_{\mathrm{M}} = 0.315$ (Planck Collaboration et al. 2020).

2. Sample, Observations, and Analysis

2.1. Sample

The sources of the Pilot Program (Neri et al. 2020) were selected from the Herschel Bright Sources (HerBS) sample (Bakx et al. 2018); they are located close to the north Galactic pole (NGP) and have flux densities in the range of $80\ \mathrm{mJy} \lesssim S_{500\,\mu\mathrm{m}} \lesssim 130\ \mathrm{mJy}$. From the 13 Herschel targets observed with NOEMA for the Pilot Program, three were resolved into multiple sources. HerBS-70 and HerBS-95 were resolved into binary systems, and HerBS-43 was resolved into two galaxies at different redshifts. This resulted in a total of 16 individual galaxies that were presented in Neri et al. (2020), 14 of which have a reliable redshift in the range of $2.08 < z < 4.05$ and were selected for follow-up VLA observations. These sources are spatially unresolved or barely resolved with the current NOEMA data with angular resolutions between 1.″2 and 6″ (Neri et al. 2020).

2.2. VLA Observations and Data Reduction

We observed the ^{12}CO(1−0)—hereafter CO(1−0)—emission line for the 14 luminous DSFGs with reliable redshifts from the z-GAL Pilot Program (Table 1). Observations were carried out using the VLA, in the C configuration (program I.D.:VLA/20A-083—P.I.: D. Riechers). We used the 0.9 cm *Ka* and *K* bands, with the correlator configured to an 8 bit sampling mode, achieving a spectral resolution of 2 MHz (i.e., 16–21 km s^{-1}), over a total bandwidth of 2 GHz in dual polarization. The observations were set up so that one of the two sidebands was centered on the expected frequency of the redshifted CO(1−0) emission line ($\nu_{\mathrm{rest}} = 115.271$ GHz) for each source. The second sideband was either positioned alongside the first to provide contiguous frequency coverage and maximize continuum sensitivity or repositioned to a significantly different frequency to obtain data with which to measure the continuum spectral index and cover faint spectral lines. Three target fields were observed with the former setting, and nine with the latter. However, the integration times were chosen to detect the CO(1−0) emission, not the underlying continuum. Note that HerBS-43a was also in the field of view for the observations of HerBS-43b, and was observed with two different frequency tunings. The data were acquired in 2020 January–May under stable atmospheric conditions and each source was observed for between 1 and 7.6 hr with 0.6 and 5.4 hr on-source integration. The 2 GHz bandwidth setup was used to maximize the potential for stacking of faint lines, while at the same time retaining sufficient spectral resolution (2 MHz) to finely sample the CO emission line for each source. The 8 bit samplers were selected to maximize sensitivity. The gain, bandpass, and flux calibrators used were 3C286, J1327+2210, J1310+3220, and J1310+3230.

The data were reduced, calibrated, and imaged using CASA V5.6.2 (Common Astronomy Software Application;[19] McMullin et al. 2007). Manual data flagging during reduction

---

[19] https://casa.nrao.edu

Table 1
The z-GAL Pilot Program Sources

Source	R.A.	Decl.	$z_{\rm spec}$	ΔV	$\mu L_{\rm IR}$	$\mu M_{\rm dust}$
	(J2000)			(km s^{-1})	$10^{12}\,L_\odot$	$10^{10}\,M_\odot$
HerBS-34	13:34:13.9	26:04:57.5	2.663	330 ± 10	40.6 ± 2.4	1.16 ± 0.07
HerBS-43a	13:24:18.8	32:07:54.4	3.212	1070 ± 90	33.4 ± 4.1	0.69 ± 0.04
HerBS-43b	13:24:19.2	32:07:49.2	4.054	800 ± 50	15.0 ± 2.0	0.45 ± 0.04
HerBS-44	13:32:55.8	34:22:08.4	2.927	520 ± 50	108.1 ± 7.8	0.7 ± 0.04
HerBS-54	13:15:40.7	26:23:19.6	2.442	1020 ± 190	23.6 ± 1.6	1.25 ± 0.12
HerBS-58	13:03:33.2	24:46:42.3	2.084	970 ± 50	17.7 ± 1.3	0.83 ± 0.06
HerBS-70E	13:01:40.3	29:29:16.2	2.308	770 ± 50	40.5 ± 5.2	0.37 ± 0.02
HerBS-70W	13:01:39.3	29:29:25.2	2.311	140 ± 20	8.7 ± 4.2	0.09 ± 0.02
HerBS-79	13:14:34.1	33:52:20.1	2.078	870 ± 70	18.1 ± 1.2	0.83 ± 0.18
HerBS-89a	13:16:11.5	28:12:17.7	2.949	1080 ± 60	28.9 ± 2.5	1.30 ± 0.07
HerBS-95E	13:43:42.7	26:39:18.0	2.972	870 ± 50	11.4 ± 1.9	0.50 ± 0.05
HerBS-95W	13:43:41.5	26:39:22.7	2.973	540 ± 30	16.1 ± 1.8	0.77 ± 0.04
HerBS-113	13:12:11.3	32:38:37.8	2.787	900 ± 200	29.6 ± 2.8	0.72 ± 0.06
HerBS-154	13:22:58.1	32:50:51.7	3.707	310 ± 40	81.3 ± 7.3	0.46 ± 0.03

Note. The coordinates and properties of the sources are taken from Neri et al. (2020), with the exception of HerBS-89a for which we include the revised values reported in Berta et al. (2021). None of the properties in this table have been corrected for gravitational magnification (μ is the magnification factor, assuming no differential lensing between the CO and dust emission). The ΔV corresponds to the mean FWHM of the CO transitions observed. The 8–1000 μm rest-frame IR luminosities ($L_{\rm IR}$) and dust masses ($M_{\rm dust}$) are those derived using the Draine & Li (2007) approach—see Neri et al. (2020) and Berta et al. (2021) for further details.

Table 2
Observed Properties of the CO(1−0) Data

Source	Moment-0 Map Properties		CO(1−0) Line Properties				
	rms[a] (Jy km s^{-1} beam^{-1})	beam[b] (arcsec^2)	spec-rms[c] (mJy)	$S_{\rm peak}$[d] (mJy)	FWHM[e] (km s^{-1})	$I_{\rm CO(1-0)}$[f] (Jy km s^{-1})	Extent of Emission[g] (arcsec^2)
HerBS-34	0.055	0.8 × 0.7	0.19	0.7 ± 0.12	593 ± 112	0.44 ± 0.11	(1.7 ± 0.4) × (0.9 ± 0.2)
HerBS-43a	0.048	1.0 × 0.9	0.13	0.3 ± 0.06	1166 ± 249	0.37 ± 0.10	(1.2 ± 0.2) × (0.9 ± 0.3)
HerBS-43b	0.016	1.3 × 1.0	0.05	0.08 ± 0.03	744 ± 290	0.064 ± 0.033	(1.1 ± 0.3) × (0.3 ± 0.6)
HerBS-44	0.047	0.9 × 0.8	0.18	0.95 ± 0.14	377 ± 63	0.38 ± 0.08	(1.1 ± 0.3) × (0.5 ± 0.2)
HerBS-54	0.055	0.8 × 0.7	0.25	0.8 ± 0.11	1087 ± 176	0.92 ± 0.19	$\lesssim$2.2 × 2.1
HerBS-58	0.046	0.9 × 0.6	0.57	2.12 ± 0.32	363 ± 64	0.82 ± 0.19	(2.1 ± 0.4) × (1.6 ± 0.3)
HerBS-70e	0.03	0.9 × 0.7	0.15	0.49 ± 0.09	622 ± 130	0.32 ± 0.09	(1.6 ± 0.3) × (1.2 ± 0.3)
HerBS-70w	0.019	0.9 × 0.7	0.15	0.83 ± 0.15	197 ± 39	0.17 ± 0.04	(2.1 ± 0.5) × (1.1 ± 0.3)
HerBS-79	0.043	0.8 × 0.6	0.34	1.24 ± 0.17	787 ± 125	1.04 ± 0.22	(2.9 ± 0.5) × (1.0 ± 0.2)
HerBS-89a	0.07	1.2 × 0.8	0.24	0.64 ± 0.09	1586 ± 247	1.08 ± 0.22	(2.1 ± 0.5) × (1.3 ± 0.4)
HerBS-95e	0.02	1.0 × 0.8	0.06	0.2 ± 0.04	658 ± 137	0.14 ± 0.04	(1.5 ± 0.3) × (0.8 ± 0.2)
HerBS-95w	0.024	1.0 × 0.8	0.19	0.95 ± 0.12	522 ± 76	0.52 ± 0.10	(2.5 ± 0.4) × (1.9 ± 0.3)
HerBS-113	0.035	1.0 × 0.7	0.32	1.46 ± 0.21	497 ± 81	0.77 ± 0.16	$\lesssim$3 × 2.8
HerBS-154	0.035	1.2 × 1.0	0.16	0.95 ± 0.11	384 ± 54	0.39 ± 0.07	(2.7 ± 0.4) × (1.7 ± 0.3)

Notes.
[a] The rms of the moment-0 maps;
[b] The beam sizes of the moment-0 maps;
[c] The rms per 100 km s^{-1} channels of the extracted spectra, based on the line-free channels;
[d] The fitted flux peak of the CO(1−0) emission line;
[e] The fitted FWHM of the CO(1−0) emission line from single Gaussian fits;
[f] The integrated line flux derived from the fit to the line;
[g] Estimates using IMFIT on the size of the CO(1−0) emission are based on the moment-0 maps, deconvolved from the beam, with the exception of HerBS-54 and HerBS-113 for which we were not able to use the single Gaussian fit of IMFIT due to their complexity. For HerBS-54 and HerBS-113 we instead provide a rough upper limit of the extent of the emission.

was necessary for most sources. The accuracy of the flux density calibration is within 10%–15%, when comparing the measured fluxes for the calibrators from our observations to the calibrator models, with a median deviation of 3.33%. Spectral cubes, continuum, and CO(1−0) moment-0 maps were created and cleaned using the TCLEAN function of CASA with a natural weighting. The spectral channel width in the cubes was set to 100 km s^{-1} and continuum maps were created using the line-free channels. The resulting moment-0 maps have spatial resolutions varying from $0\farcs9 \times 0\farcs6$ to $1\farcs2 \times 1\farcs0$ and rms noise levels between 16 and 55 μJy km s^{-1} beam^{-1} (Table 2). For those sources where the underlying continuum is detected, we performed continuum subtraction for the spectral cubes using the line-free channels. Two continuum images were produced for the sources, with the exception of the three sources with continuous frequency coverage between the two sidebands for which only a single continuum image is produced.

2.3. Spectral Analysis

In order to obtain the best quality CO(1−0) spectra, we follow an iterative process for defining the extraction region used. Starting with a 1″ circular aperture centered on the source position, we extract initial spectra, from which we define the line channels to be used for the moment-0 maps. Once the moment-0 map is created, we define new extraction regions based on the 2σ contours of the map. We repeat the steps of selecting the line channels to be used for the moment-0 maps and defining the 2σ contour extraction region, until the 2σ contour converges. To achieve a higher signal-to-noise ratio (S/N) and retrieve the full information on the extent of the emission as best as possible, the total line intensity maps were created directly from the *uv* data and cleaned using TCLEAN in CASA. In Figure 1, we present the extracted spectra and moment-0 maps for each source. The properties of the extracted CO(1−0) lines are listed in Table 2 together with the rms noise levels and the spatial resolution of the moment-0 maps. For sources where a clear double peak is seen in the line profile, we fit with both single and double Gaussian components; however, we find that the integrated flux does not change significantly between the two. As the more complex fit is not required by the data and will only increase the uncertainties due to the larger number of fitting parameters, we chose to only use the results of the simpler, single Gaussian fit.

2.4. Continuum Analysis

As the aim of the observations was to detect the CO(1−0) emission, and the observations were not designed to detect the continuum, the majority of our sample is not detected in the continuum, with the exception of four sources, namely, HerBS-43a, HerBS-43b, HerBS-54, and HerBS-70E. For these sources, we used the 2D Gaussian fitting tool IMFIT of CASA to retrieve the total continuum flux density. In Table 3, we give the continuum flux densities, the rms values, and the corresponding frequencies. The radio continuum emission for the four sources detected is displayed as white contours on the moment-0 maps of Figure 1. For the sources where no continuum emission was detected, Table 3 lists the rms noise level of each map.

Within the field of HerBS-44, a serendipitous source is detected in the radio continuum (at 29 and 38 GHz) at a distance of ∼34″ from the main source. The position of the source is at R.A. 13:32:57.8, decl. +34:22:27.0 (J2000.0), and the continuum fluxes are reported in Table 3 under the source name HerBS-44s. A likely counterpart to this source is FIRST J133257.7+342227 with a separation of 0.″36, or NVSS J133257+342228 at a separation of 1″.

3. Results

In this section, we present the initial results on the observed CO(1−0) line emission (Section 3.1), and the radio continuum measurements (Section 3.2) of our sample.

3.1. Observed Emission Line Properties

All sources are detected in CO(1−0) with at least 5σ significance for the integrated line flux. Here we provide an overview of the observed properties of our sample, with more detailed descriptions for the individual sources reported in Appendix A.

In Figure 1 we compare the CO(1−0) line to the higher-*J* CO lines detected in 2 and 3 mm with NOEMA (Neri et al. 2020). Specifically, we compare the FWHM from the Gaussian fit to the CO(1−0), with the average of the FWHM from the respective Gaussian fits to the higher-*J* transitions (expressed as ΔV in Neri et al. 2020). To quantify the difference, we use the relative difference between the two, expressed as $|\mathrm{FWHM} - \Delta \mathrm{V}|/\Delta \mathrm{V}$. We find that the line profiles are similar for most sources in our sample, with 12/14 sources having a CO(1−0) FWHM consistent within 50% of the ΔV from Neri et al. (2020) for the higher-*J* transitions. The two sources with a significant difference in line widths are HerBS-34 with a ratio of $\mathrm{FWHM}/\Delta \mathrm{V} = 1.8 \pm 0.3$, and HerBS-58 with a ratio of $\mathrm{FWHM}/\Delta \mathrm{V} = 0.4 \pm 0.1$. The large ratio of HerBS-34 is most likely due to the low S/N of the CO(1−0) observations. The case of HerBS-58 is more complex. When comparing to the previously observed CO(3–2) and [C I]($^3P_1-^3P_0$) in Figure 2 it becomes apparent that we are only detecting part of the line emission in CO(1−0). Specifically, we are only detecting the red component of the line. Consequently, as we are only fitting the red component, this also leads to an underestimation of the error on the FWHM/ΔV. When comparing the CO(1−0) moment-0 map to the resolved velocity map of [C I]($^3P_1-^3P_0$) in Neri et al. (2020), we find that the CO(1−0) is located in the redshifted western region, with no emission covering the blueshifted eastern part of the [C I] emission, consistent with the lack of emission seen for the expected blue component of the line. A more detailed analysis of the CO and [C I] emission in HerBS-58, will be provided in D. Ismail et al. 2023, (in preparation) based on new high-angular resolution NOEMA data.

The resolution of ∼1″ achieved with the VLA has allowed for all sources to be at least partially resolved (see Table 2 and Figure 1). Half of the sample shows compact to somewhat extended emission over 9–18 kpc scales. For the other 7/14 sources extended and complex structure is revealed, over scales of 18–25 kpc, with HerBS-54, HerBS-58, HerBS-79, HerBS-89a, HerBS-113, and HerBS-154 showing multiple peaks in their emission, while HerBS-95W has a single peak and extends over 20 kpc. The complex, multi-peak structure observed for these sources is a possible indicator for lensing, as shown in Berta et al. (2021) for HerBS-89a. However, we are not able to perform a detailed lensing analysis in order to confirm this with the current data. A brief discussion on this point is provided in Appendix B.

3.2. Radio Continuum

As reported in Section 2, due to the limited sensitivity of the VLA data, the majority of the sample is not detected in the continuum, with the exception of four sources. The typical rms levels are between ∼4 and 45 μJy beam^{-1} in the observed frequency range of 20–38 GHz. In Table 3 we give the continuum properties of the full sample. The four sources detected in the high-frequency radio continuum are HerBS-43a, HerBS-43b, HerBS-54, and HerBS-70E; the continuum emission is displayed as white contours in the respective panels in Figure 1.

Sources HerBS-43a and HerBS-43b are similarly compact in the 22.2 GHz (rest frame 93.5 and 112.2 GHz, respectively) continuum than in the CO(1−0) emission, but we observe a small offset of ∼0.″5 between the continuum and CO(1−0) emission for both sources. Similarly, the continuum of HerBS-

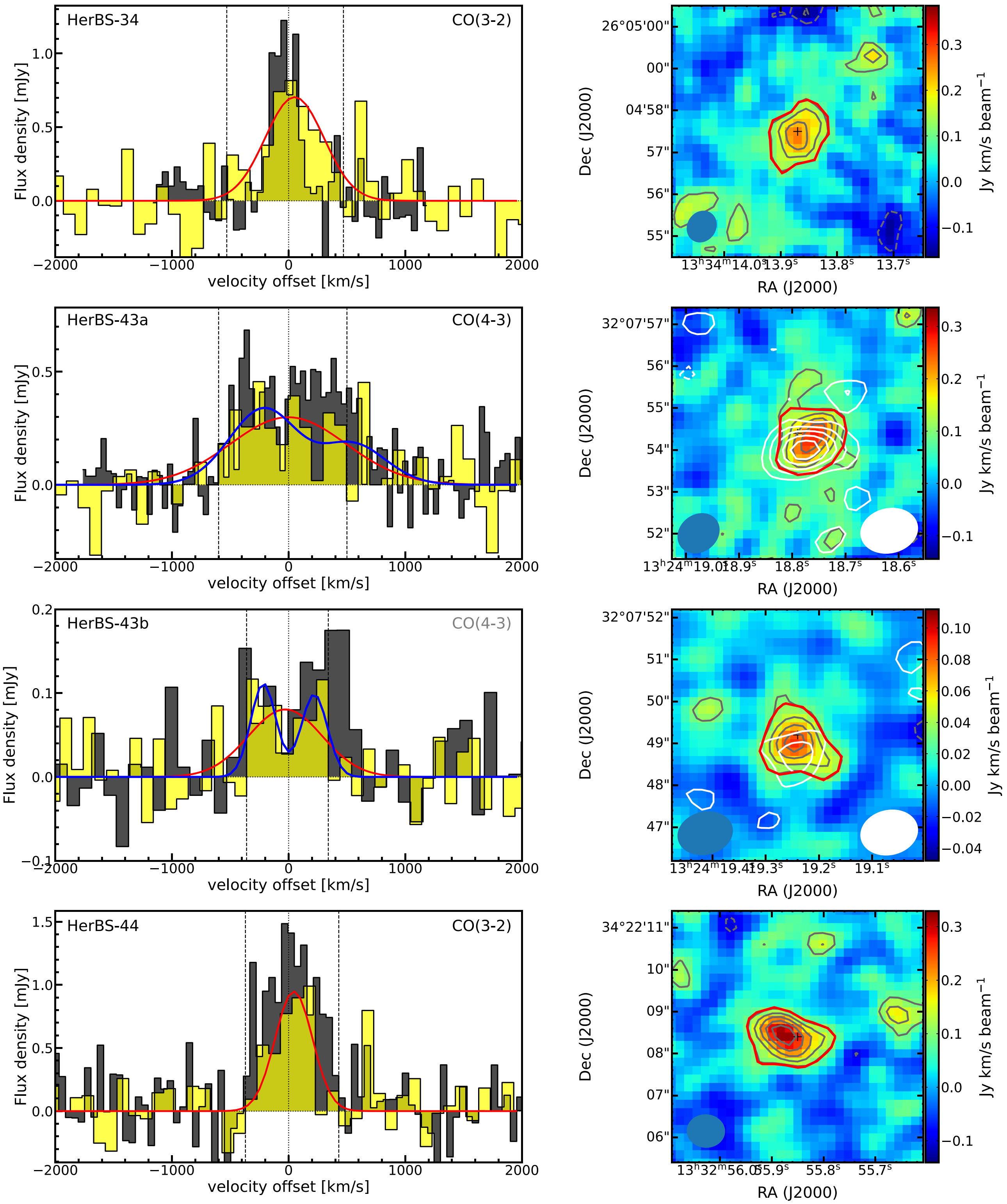

Figure 1. CO(1−0) spectra (left), moment-0 (right) for each source in our sample. The source names are indicated on the top of the left panels. Each CO(1−0) emission line is plotted in yellow and centered at the zero velocity corresponding to the redshift of the source (see Table 1), and the Gaussian fits to the lines are shown with red curves. For comparison, we plot the next lowest-*J* CO line from Neri et al. (2020) in gray, normalized to 1.5× the peak of the CO(1−0) line to show the respective line profiles with more clarity. The comparison line used is indicated on the top right of each plot. The moment-0 map contours are plotted starting at 2σ and increase in steps of 1σ, where the 1σ noise levels for each source are listed in Table 2. The symmetric negative contours are also shown, with dashed curves. The synthesized beam is shown in the lower left corner of each moment-0 map. The maps are centered on the positions listed in Table 1. For the sources detected in continuum (HerBS-43a, HerBS-43b, HerBS-54, and HerBS-70E), we overplot in white contours the continuum emission on the moment-0 maps, and the corresponding synthesized beam on the lower right corner. The continuum contours start at 2σ and increase in steps of 1σ, with the exception of HerBS-70E for which we plot contours at 2σ, 5σ, 10σ, 30σ, and 40σ (see Table 3). The red polygon on the moment-0 maps corresponds to the region from which we extracted the spectra.

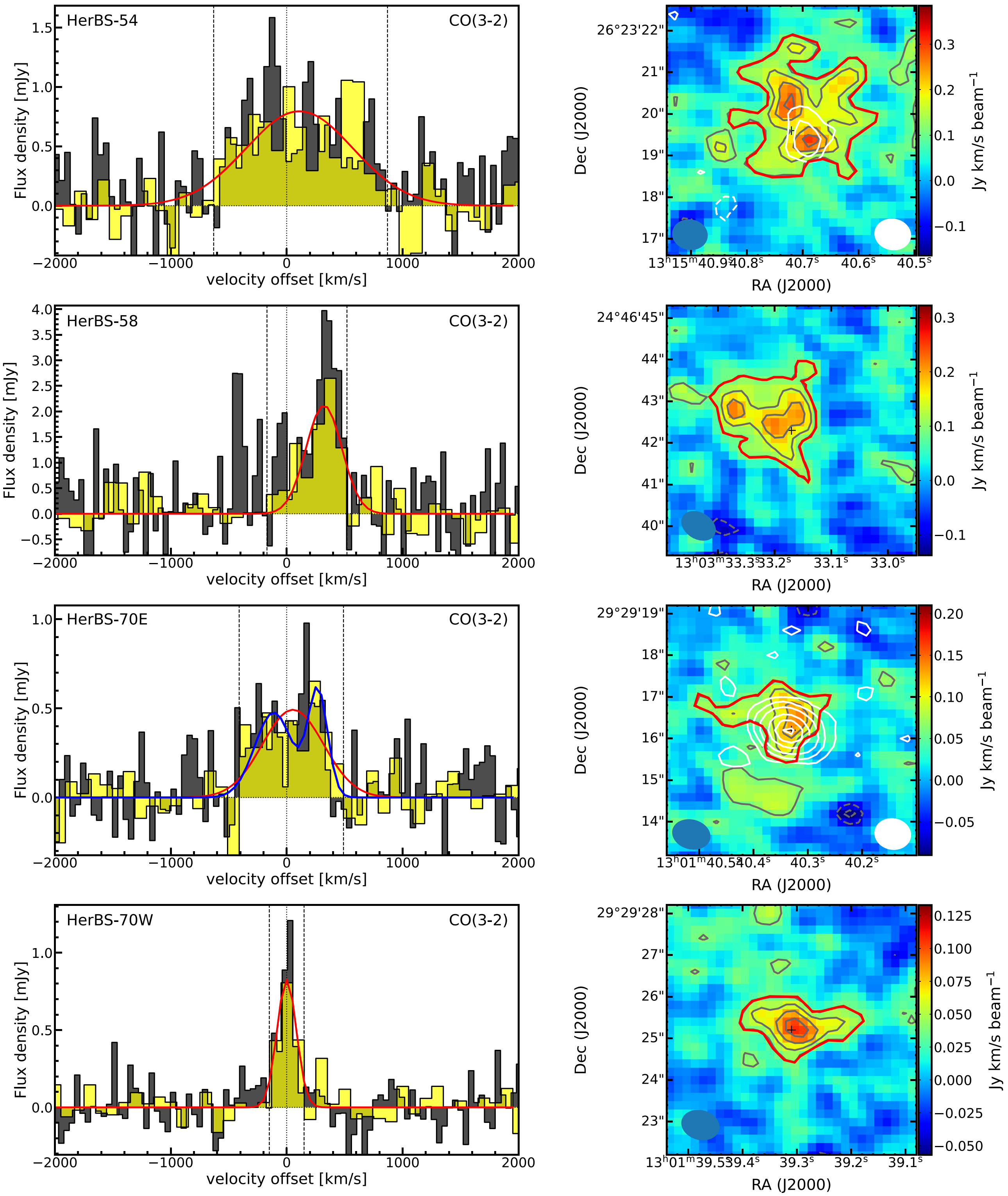

Figure 1. (Continued.)

70E, detected at 27.1 and 34.8 GHz (rest-frame 89.6 GHz and 115.1 GHz) is also somewhat offset with respect to the CO(1−0) emission, and displays a more compact morphology. Interestingly, HerBS-54, detected at 33.0 GHz (rest frame 113.6 GHz) has continuum emission that is aligned with only the south peak of the CO(1−0) emission, although there is some extension toward the north. This could be a result of the north component being fainter in the continuum and therefore not detected in these observations.

For the sources detected in the radio continuum we define simple spectral energy distribution (SED) models, in which we use the modified blackbody (MBB) fits done to the NOEMA continuum data in Neri et al. (2020), with correction for the cosmic microwave background (CMB)

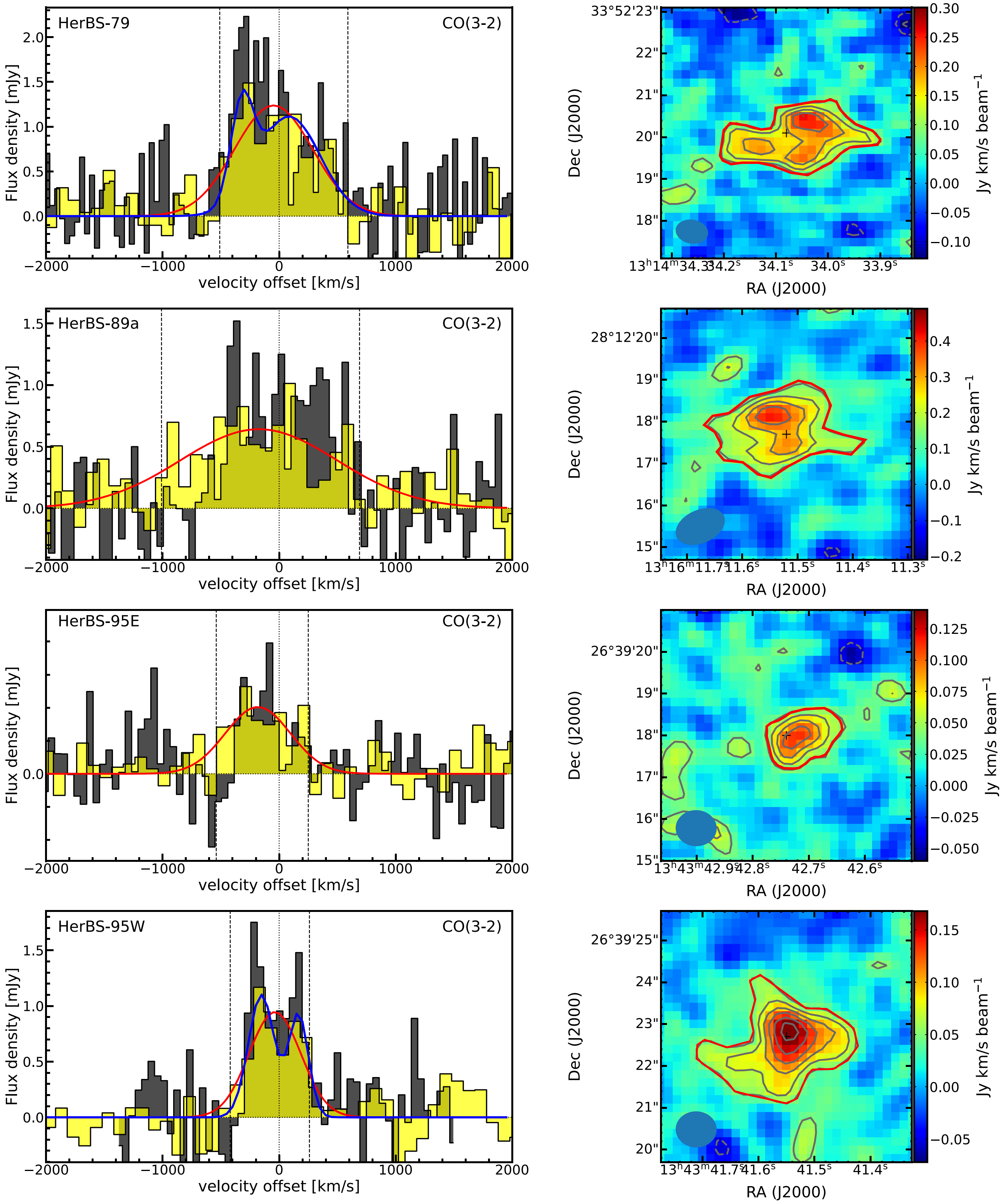

Figure 1. (Continued.)

following da Cunha et al. (2013), and simply add a power-law spectrum of $S_\nu \propto \nu^{-0.8}$ representing the synchrotron emission due to star formation (SF synchrotron), normalized on the basis of the radio/far-IR correlation taking into account the redshift evolution described in Delhaize et al. (2017) and the IR emission derived using the DL07 model (Draine & Li 2007) as reported in (Neri et al. 2020) (see Table 1). We show these SEDs in Figure 3.

In the case of HerBS-43a, the continuum at 22.2 GHz lies on the expected SF synchrotron power law, while the upper limits at 27.2 and 37.4 GHz are also consistent. Although they lie above the expected emission based on the Delhaize et al. (2017)

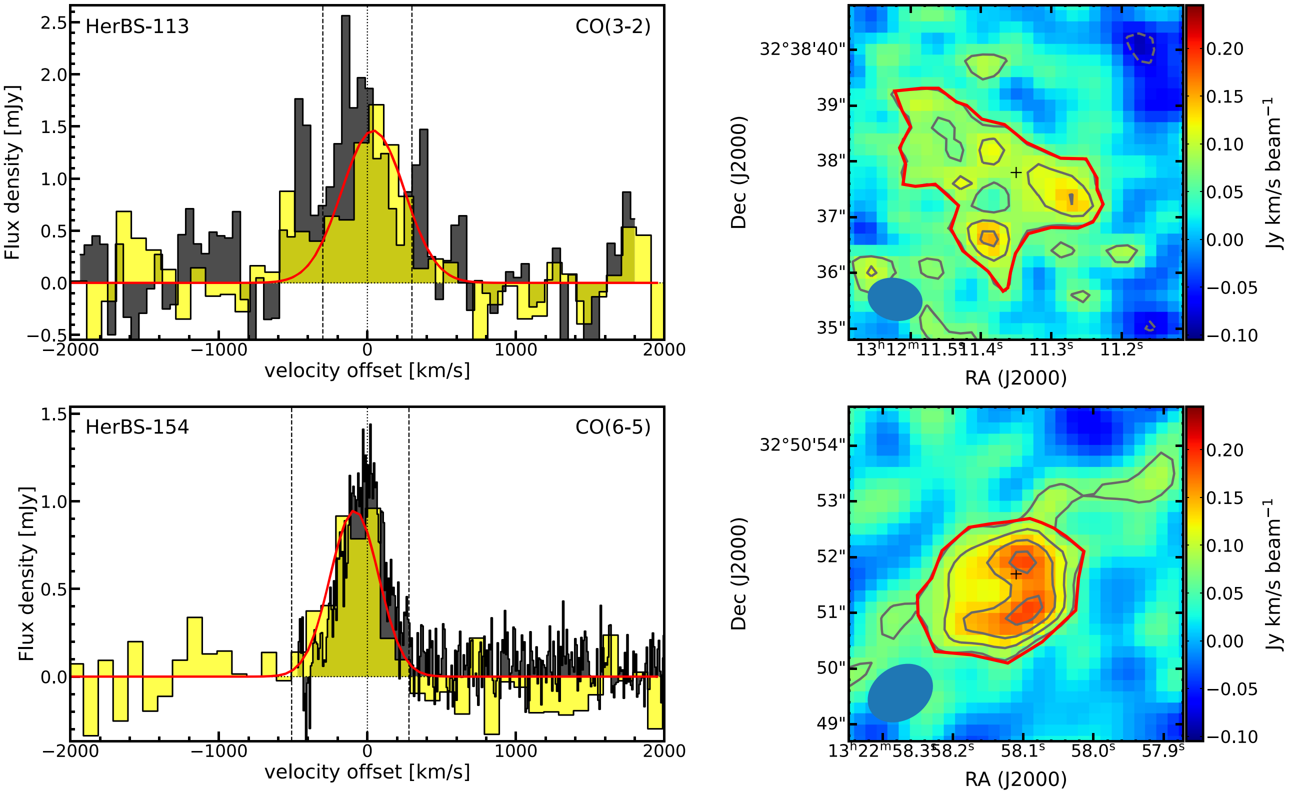

Figure 1. (Continued.)

Table 3
Continuum Measurements

Source	$\nu_{\rm cen}$ (GHz) LSB	$\nu_{\rm cen}$ (GHz) USB	rms (mJy beam^{-1}) LSB	rms (mJy beam^{-1}) USB	$S_{\rm cont}$ (mJy) LSB	$S_{\rm cont}$ (mJy) USB
HerBS-34	32.02		0.011		⋯	
HerBS-43a	27.3	37.45	0.014	0.018	⋯	⋯
HerBS-43a	22.24		0.004		0.024 ± 0.007	
HerBS-43b	22.24		0.004		0.019 ± 0.003	
HerBS-44	29.16	38.51	0.016	0.023	⋯	⋯
HerBS-44s	29.16	38.51	0.037	0.045	0.77 ± 0.04	0.65 ± 0.08
HerBS-54	33.06		0.009		0.072 ± 0.013	
HerBS-58	28.80	37.31	0.014	0.02	⋯	⋯
HerBS-70E	27.11	34.78	0.01	0.01	0.60 ± 0.02	0.47 ± 0.02
HerBS-70W	27.11	34.78	0.01	0.01	⋯	⋯
HerBS-79	28.73	37.51	0.01	0.015	⋯	⋯
HerBS-89a	29.18	38.49	0.02	0.05	⋯	⋯
HerBS-95E	28.95	38.5	0.008	0.01	⋯	⋯
HerBS-95W	28.95	38.5	0.008	0.01	⋯	⋯
HerBS-113	30.37	38.5	0.016	0.022	⋯	⋯
HerBS-154	19.15	24.42	0.022	0.01	⋯	⋯

Note. The source HerBS-43a was observed with two different tunings. The results for HerBS-89a are from Berta et al. (2021). HerBS-44s is a serendipitous source detected in the radio continuum located ∼34″ to the northeast of HerBS-44 at R.A. 13:32:57.8, decl. +34:22:27.0 (J2000.0).

relation, HerBS-43b and HerBS-54 have flux densities that are compatible with the synchrotron emission due to star formation as they are in agreement with expectations based on the Magnelli et al. (2015) relation. However, we note that measurements at lower frequencies (e.g., 4–8 GHz) would be useful to further assess the slope and derive the properties of the radio emission in these DSFGs, and in particular, to estimate the contribution of the free–free (Bremsstrahlung) emission with a power-law radio spectrum of $S_\nu \propto \nu^{-0.1}$ that contributes significantly at higher frequencies (e.g., Condon 1992; Thomson et al. 2014). All the sources with only upper limits in the radio continuum are compatible with the synchrotron emission levels derived from the radio/far-IR relationship.

In the case of HerBS-70E, the flux densities are well above the expected level of the synchrotron emission due to star formation. This clearly indicates the presence of a radio-

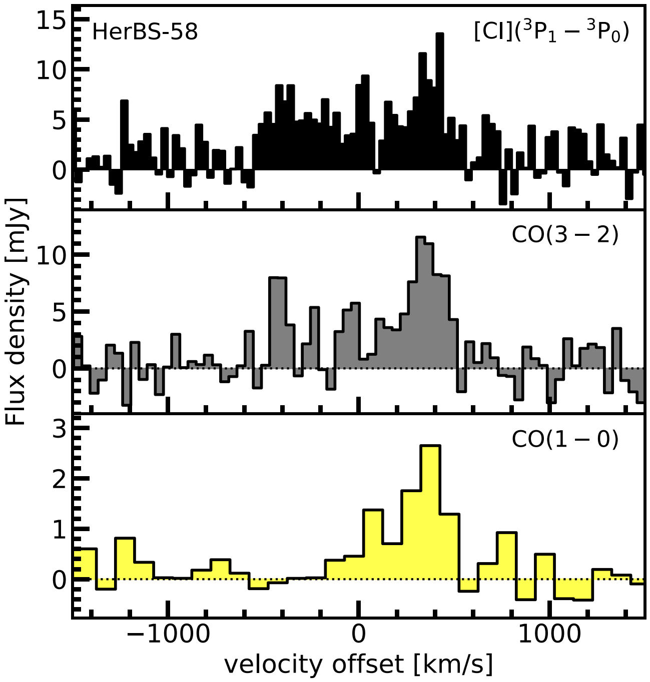

Figure 2. A comparison of the detected emission lines of HerBS-58. The lines plotted are indicated on the upper left of each panel. Both the CO(3–2) and [C I] spectra have additional emission at negative velocities, not seen in the CO(1−0) spectra.

luminous active galactic nucleus (AGN) in this source (see Figure 3). HerBS-70E was also detected in the FIRST survey (Becker et al. 1995) at 1.4 GHz and with LOFAR at 126–173 MHz (Hardcastle et al. 2016), tracing the increase of the radio flux density at these lower frequencies (corresponding to 4.63 GHz and 416–572 MHz in the rest frame), including the expected turnover of the radio AGN emission. Based on the 1.4 GHz data we estimate a radio luminosity of $L_{1.4\rm GHz} = 2.4 \times 10^{26}$ W Hz^{-1}, placing it among typical radio-luminous AGN at these redshifts. A more detailed analysis of this source will be presented in a separate paper.

4. Discussion

In this discussion, we use the observed CO(1−0) line properties to determine the molecular gas properties of our sample of luminous DSFGs, namely, the CO luminosities and masses (Section 4.1), the gas properties, including the gas depletion time that is compared to other samples previously observed in CO(1−0) (Section 4.2), and the gas-to dust mass ratios (Section 4.3). In Section 4.4, we estimate the CO line ratios by combining the CO(1−0) measurements with the previously observed higher-J CO transitions from Neri et al. (2020), and in Section 4.5, we analyze the CO spectral line energy distribution (SLED) of each source in our sample with radiative transfer modeling. An important caveat that must be noted, and could affect most if not all of the points in this discussion, is the likelihood of our observations missing extended CO(1−0) emission. This would increase the line fluxes and luminosities, but it is not clear by how much, and how significant that difference could be.

4.1. CO Luminosities, Molecular Gas Masses, and the Choice of α_{CO}

The direct measure of the CO(1−0) emission allows for the estimation of the line luminosity, $L'_{\rm CO(1-0)}$, and molecular gas masses, $M_{\rm H_2}$, without the uncertainty of conversion from higher-J CO transitions. We estimate these values following the standard equations given below (e.g., Carilli & Walter 2013):

$$L'_{\rm CO} = 3.25 \times 10^7 \times \frac{S_{\rm CO}\,\Delta v_{\rm CO}\,D_{\rm L}^2}{\nu_{\rm CO,rest}^2 \times (1+z)}\ [{\rm K\ km\ s^{-1}\ pc^{-2}}],$$

$$M_{\rm H_2} = \alpha_{\rm CO} \times L'_{\rm CO(1-0)}\ [M_\odot],$$

where $S_{\rm CO}\,\Delta v_{\rm CO}$ is the measured flux of the line in jansky times kilometers per second, $D_{\rm L}$ is the luminosity distance in megaparsec, $\nu_{\rm CO,rest}$ is the rest frequency of the line in gigahertz, and $\alpha_{\rm CO}$ is the CO(1−0)−H$_2$ conversion factor.

The estimation of $M_{\rm H_2}$ remains uncertain even with the direct measure of the CO(1−0) emission, due to the dependence on $\alpha_{\rm CO}$, which itself is dependent on other properties of the galaxies, such as metallicity, that are difficult to determine over a large sample of galaxies, especially at high redshifts (see, e.g., Bolatto et al. 2013; Dunne et al. 2021). Historically, studies of classical submillimeter galaxies (SMGs) have assumed an $\alpha_{\rm CO} = 0.8\,M_\odot\,({\rm K\ km\ s^{-1}\ pc^2})^{-1}$ (see review by Carilli & Walter 2013), in agreement with the dynamical constraints on the $\alpha_{\rm CO}$ in local starburst galaxies placing it within the range of 0.8–1.5 $M_\odot\,({\rm K\ km\ s^{-1}\ pc^2})^{-1}$ (e.g., Downes & Solomon 1998; Genzel et al. 2010). Normal star-forming galaxies seem to have an $\alpha_{\rm CO} \sim 4\,M_\odot\,({\rm K\ km\ s^{-1}\ pc^2})^{-1}$ (e.g., Carilli & Walter 2013; Genzel et al. 2015; Tacconi et al. 2013, 2018) consistent with Galactic studies (e.g., Bolatto et al. 2013). More recently a study on Herschel-selected galaxies (HSGs) using multiple gas tracers to calibrate the gas mass, found an average $\alpha_{\rm CO} = 3\,M_\odot\,({\rm K\ km\ s^{-1}\ pc^2})^{-1}$ (Dunne et al. 2021). For the purposes of this discussion, we chose to use the results of Dunne et al. (2021), and assume an $\alpha_{\rm CO} = 3\,M_\odot\,({\rm K\ km\ s^{-1}\ pc^2})^{-1}$, but in addition, we examine the range of results possible when assuming the two extremes of $\alpha_{\rm CO} = 0.8$–$4.3\,M_\odot\,({\rm K\ km\ s^{-1}\ pc^2})^{-1}$. We note that during the final stages of this study, a more updated analysis of the $\alpha_{\rm CO}$ was presented in Dunne et al. (2022), using a much larger sample of 407 galaxies spanning up to $z \sim 6$, and found $\alpha_{\rm CO}$ values consistent with those of Dunne et al. (2021), assumed in our analysis. We also note that in a detailed high-resolution study of a high-z luminous HSG, Dye et al. (2022) estimated the gas mass of the galaxy following different tracers and methods, including from CO(1−0) assuming $\alpha_{\rm CO} = 3\,M_\odot\,({\rm K\ km\ s^{-1}\ pc^2})^{-1}$, and found a surprising agreement between the resulting gas masses.

The estimated CO(1−0) luminosities and gas masses for our sample are given in Table 4. We find molecular gas masses of $1.2-13.2 \times 10^{11} M_\odot$, with no corrections made for the possible magnification due to gravitational lensing. The sources with the largest values ($\geqslant 5.4 \times 10^{11}$) are all identified to have extended and complex structure and are likely magnified. For HerBS-89a, correction for gravitational lensing ($\mu = 5$) reduces the molecular gas mass from $(13.2 \pm 2.7) \times 10^{11}$ to $(2.6 \pm 0.5) \times 10^{11}\ M_\odot$ (see also Berta et al. 2021). The large molecular gas masses measured are consistent with the necessary conditions to support the SFRs of such galaxies,

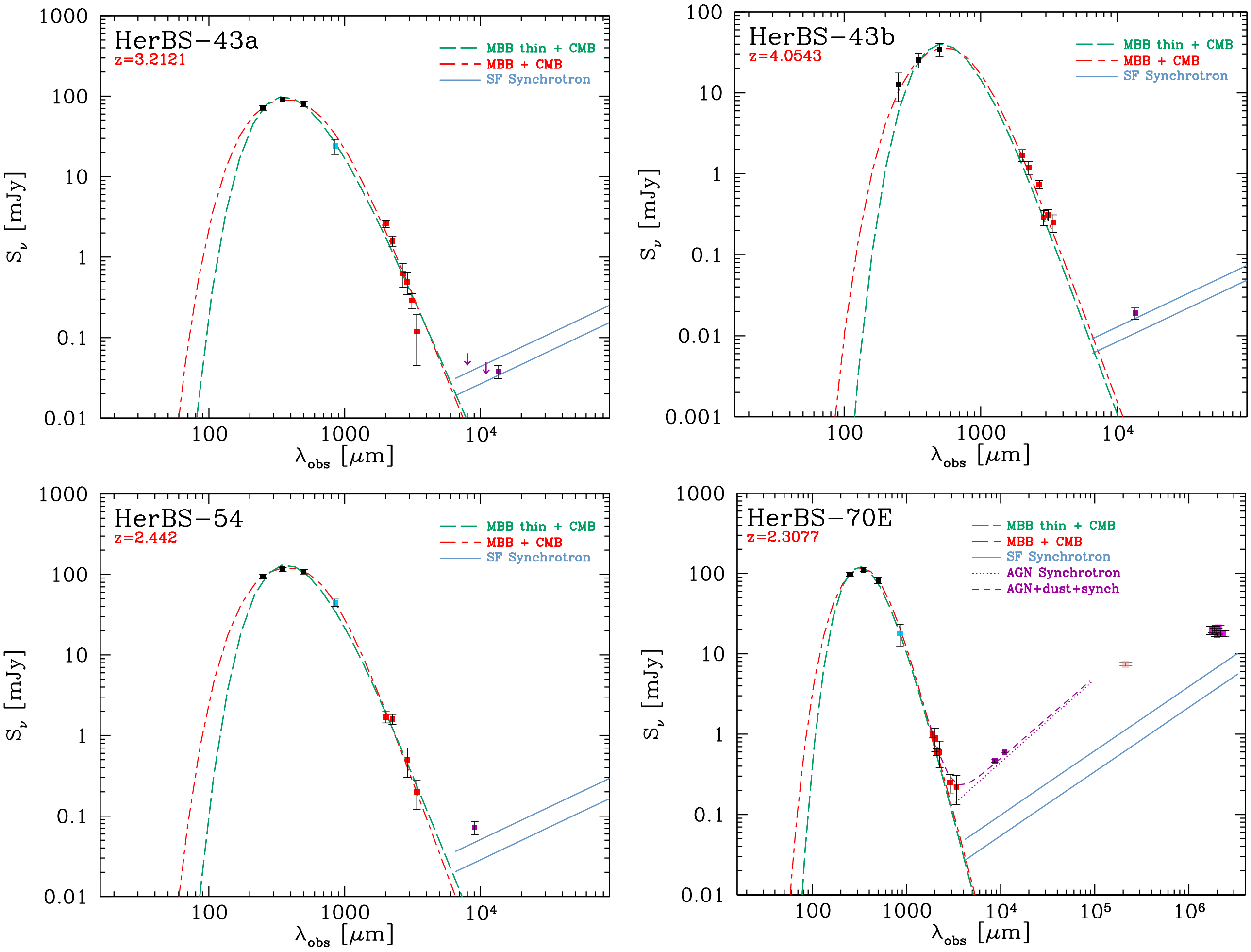

Figure 3. Observed SEDs for the four sources detected in the radio continuum, HerBS-43a, HerBS-43b, HerBS-54, and HerBS-70E (from top left to bottom right panel). The data include SPIRE and SCUBA-2 flux densities (black and blue dots; Bakx et al. 2018) and NOEMA continuum flux densities at 2 and 3 mm (red dots; Neri et al. 2020); the VLA measurements at 22–38 GHz (13–7.8 mm) are shown as purple dots and the 3σ upper limits as purple arrows. The fits are based on MBB dust models (green and red lines) including corrections for the effects of the CMB (see the text for details). The light-blue continuous lines represent the synchrotron emission due to star formation, with a fixed spectral index $\alpha = -0.8$, normalized on the basis of two radio/far-IR correlations derived by Delhaize et al. (2017) (lower line), and Magnelli et al. (2015) (upper line). In the case of HerBS-70E, we also plot the synchrotron emission due to the AGN (purple dotted line), and the sum of all components (purple dashed line), and additional radio data from the FIRST survey at 1.4 GHz and LOFAR at 126–173 MHz, for comparison.

Table 4
Derived Properties of the Molecular Gas

Source	$(\mu)L'_{\rm CO}$ (10^{11} K km s^{-1} pc^{2})	$(\mu)M_{\rm H_2}$ (10^{11} $M_\odot$)	$t_{\rm dep}$ (10^{2} Myr)
HerBS-34	1.5 ± 0.4	4.5 ± 1.2	1.1 ± 0.3
HerBS-43a	1.7 ± 0.5	5.1 ± 1.5	1.5 ± 0.5
HerBS-43b	0.4 ± 0.2	1.2 ± 0.6	0.8 ± 0.4
HerBS-44	1.5 ± 0.3	4.5 ± 0.9	0.4 ± 0.1
HerBS-54	2.7 ± 0.6	8.1 ± 1.8	3.4 ± 0.8
HerBS-58	1.8 ± 0.4	5.4 ± 1.2	3.1 ± 0.7
HerBS-70E	0.9 ± 0.2	2.7 ± 0.6	0.7 ± 0.2
HerBS-70W	0.5 ± 0.1	1.5 ± 0.3	1.7 ± 0.9
HerBS-79	2.3 ± 0.5	6.9 ± 1.5	3.8 ± 0.9
HerBS-89a	4.4 ± 0.9	13.2 ± 2.7	4.6 ± 1.0
HerBS-95e	0.6 ± 0.2	1.8 ± 0.6	1.6 ± 0.6
HerBS-95w	2.2 ± 0.4	6.6 ± 1.2	4.1 ± 0.9
HerBS-113	2.9 ± 0.6	8.7 ± 1.8	2.9 ± 0.7
HerBS-154	2.3 ± 0.4	6.9 ± 1.2	0.9 ± 0.2

Note. Where μ is the magnification factor due to gravitational lensing, $L'_{\rm CO}$ is the CO(1−0) luminosity, $M_{\rm H_2}$ is the molecular gas mass, and $t_{\rm dep}$ is the depletion time.

and are in agreement with literature results for luminous DSFGs (e.g., Tacconi et al. 2008; Ivison et al. 2011; Bothwell et al. 2013; Aravena et al. 2016; Harrington et al. 2021).

4.2. Molecular Gas Depletion Times and Star Formation Efficiencies

Two parameters of interest when investigating the molecular gas properties of galaxies, are the star formation efficiency (SFE) and its inverse, the gas depletion time ($t_{\rm dep}$). The SFE is a measure of the efficiency of star formation given the molecular gas reservoir available, and can be expressed as SFE = SFR/$M_{\rm gas}$, where SFR[$M_\odot$ yr^{-1}] $= 1.09 \times 10^{-10}$ $L_{\rm IR}[L_\odot]$, and $L_{\rm IR}$ is the IR luminosity at rest frame 8–1000 μm (Kennicutt 1989, corrected for a Chabrier (2003) initial mass function). The $t_{\rm dep}$ is a measure of the time it would take for the molecular gas to be depleted by the current SFR, assuming that the SFR will remain constant throughout this period and that no other processes (such as gas accretion or outflows) affect the gas reservoir.

To compare the line emission properties of our sample to previously observed DSFGs at low and high redshifts, we plot $L_{\rm IR}$ as a function of $L'_{\rm CO(1-0)}$ and the ratio of $L'_{\rm CO(1-0)}/L_{\rm IR}$ in

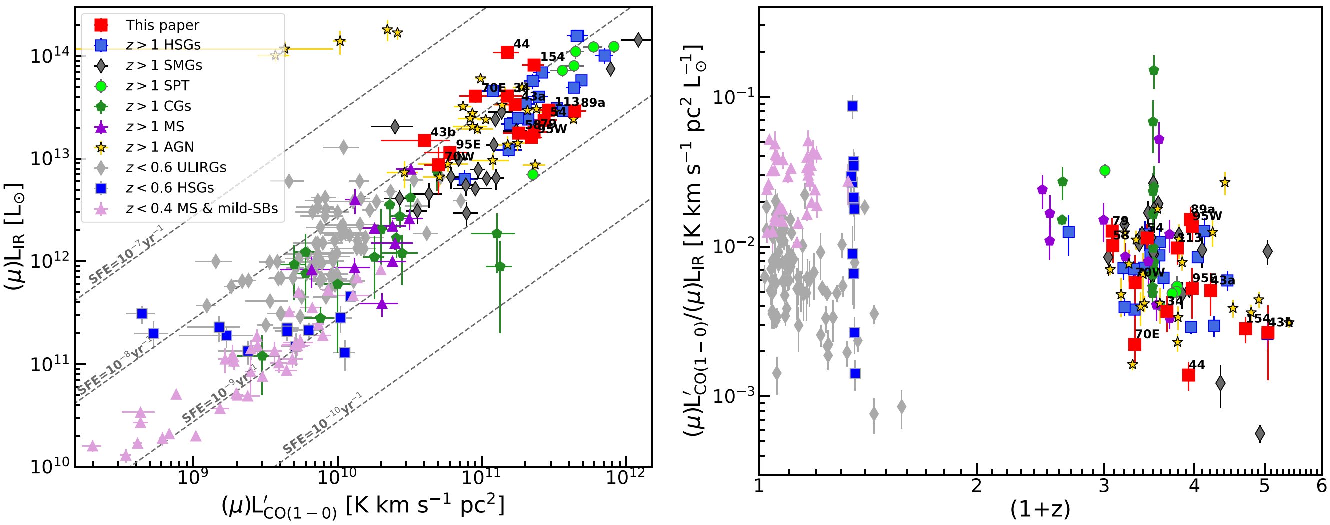

Figure 4. (left) IR luminosity ($L_{\rm IR}$; 8–1000 μm) as a function of $L'_{\rm CO(1-0)}$ for the DSFGs reported in this paper (shown as red squares and identified by their names). For comparison we also plot low and high-redshift DSFGs from the literature, categorized as SMGs, HSGs, galaxies from the SPT survey, cluster galaxies (CGs), galaxies on the MS, DSFGs hosting AGN and ULIRGs (see Section 4.2 for a detailed list of references). Only sources with reported CO(1−0) emission lines have been included to avoid uncertainties in estimating the CO(1−0) luminosities from higher-J transitions. Trends of constant SFE values are plotted with gray dashed lines. (right) The $L'_{\rm CO(1-0)}/L_{\rm IR}$ ratio as a function of $(1+z)$. In both plots, corrections for amplification were not applied to the IR and CO luminosities for the gravitationally amplified galaxies.

Figure 4. For this comparison we only include DSFGs with measured CO(1−0) and we split the sources based on redshift and in the following categories: classical SMGs selected at 850 μm and/or 1200 μm (see compilation in Carilli & Walter 2013), with CO(1−0) measurements from Riechers et al. (2011a, 2011d), Swinbank et al. (2011), Dannerbauer et al. (2019), Lestrade et al. (2011) ,Harris et al. (2010), Carilli et al. (2010), Ivison et al. (2011), Thomson et al. (2012), and Sharon et al. (2016); galaxies from the South Pole Telescope (SPT) survey (e.g., Weiß et al. 2013; Spilker et al. 2014), and with CO(1−0) measurements presented in Aravena et al. (2013, 2016); HSGs from surveys such as Herschel-ATLAS (e.g., Valiante et al. 2016; Maddox et al. 2018) and the HerBS catalog (Bakx et al. 2018), with CO(1−0) measurements from Harris et al. (2012), George et al. (2013), and Bakx et al. (2020b); galaxies from cluster studies (Rudnick et al. 2017; Wang et al. 2018); galaxies on the main sequence (MS; Aravena et al. 2014; Villanueva et al. 2017); high-z DSFGs hosting AGN (from the compilations of Harris et al. 2012; Carilli & Walter 2013; Sharon et al. 2016; Penney et al. 2020); and ULIRGs (Solomon et al. 1997; Chung et al. 2009; Combes et al. 2011).

In Figure 4 we can see that our sample falls within the scatter of high-redshift DSFGs, without much distinction between the different selection methods. Furthermore, although there is an apparent $L_{\rm IR}$–$L'_{\rm CO(1-0)}$ correlation for most sources, it is worth noting that the scatter corresponds to a factor of ∼10 in SFEs. When taking the ratio of $L'_{\rm CO(1-0)}/L_{\rm IR}$ with redshift the comparison among samples becomes somewhat clearer as the effects of magnification are removed. The luminosity ratios of high-redshift SMGs, HSGs, AGN, and SPT galaxies, cover the same range as lower redshift ULIRGs, while there is quite some overlap between these high-redshift luminous DSFGs and MS galaxies at those redshifts.

Although, the ratios of $L'_{\rm CO(1-0)}/L_{\rm IR}$ (or reverse) can be interpreted as a proxy to $t_{\rm dep}$ (or SFE) allowing for comparisons without the interference of $\alpha_{\rm CO}$ assumptions, such comparisons, especially between different populations, remain limited precisely due to the fact that the $\alpha_{\rm CO}$ could vary significantly among the range of the sources examined.

To further examine the $t_{\rm dep}$ of our sample we plot in Figure 5 $t_{\rm dep}$ as a function of redshift, comparing to the high-redshift luminous DSFGs for which it is more likely that a similar value of $\alpha_{\rm CO}$ could apply. We also plot the range of $t_{\rm dep}$ covered by MS galaxies from the relation presented in the Tacconi et al. (2020) review. To examine the effect that the assumed $\alpha_{\rm CO}$ can have on the $t_{\rm dep}$ values, we include in the plotted error bars the range of $t_{\rm dep}$ that results from assuming $\alpha_{\rm CO} = 0.8$ and 4.3.

The range in $t_{\rm dep}$ that we find for our sample is consistent with what is seen for the luminous DSFGs at the same redshifts. Furthermore, we observed the decreasing trend of $t_{\rm dep}$ with redshift that has been previously observed for the general population of DSFGs (see review by Tacconi et al. 2020).

Overall, we find a $t_{\rm dep}$ of 40–460 Myr for our sources (see Table 4). These values place our sample both on and below the MS values for the redshift range covered, demonstrating that luminous DSFGs from Herschel-selected samples, include both normal and star-bursting galaxies (see also Berta et al. 2021).

4.3. Gas-to-dust Ratios

We use the dust masses ($M_{\rm dust}$) derived for our sample by Neri et al. (2020) using Draine & Li (2007) templates (see Table 1), to estimate the gas-to-dust ratio ($M_{\rm H_2}/M_{\rm dust}$). We find a wide range of values, $M_{\rm H_2}/M_{\rm dust} = 27$–167, with a mean of ∼82 (see the solid histogram in Figure 6). For comparison, $z \sim 0.3$ HSGs have ratios of 64–261, with a mean of 128^{+54}_{-35} (Dunne et al. 2021), these values remain consistent with the larger sample of DSFGs of Dunne et al. (2022) at $z < 6$. For nearby star-forming galaxies, the ratio is ∼70 (Sandstrom et al. 2013). Although the majority of our sample is in agreement with previous measurements of the gas-to-dust ratio, HerBS-43b, HerBS-95E, and HerBS-34 have surprisingly low ratios of 27, 36, and 39, respectively. These low ratios could be a result of variation of $\alpha_{\rm CO}$ among the sample, or due to the presence of an AGN contaminating the SED and artificially elevating the

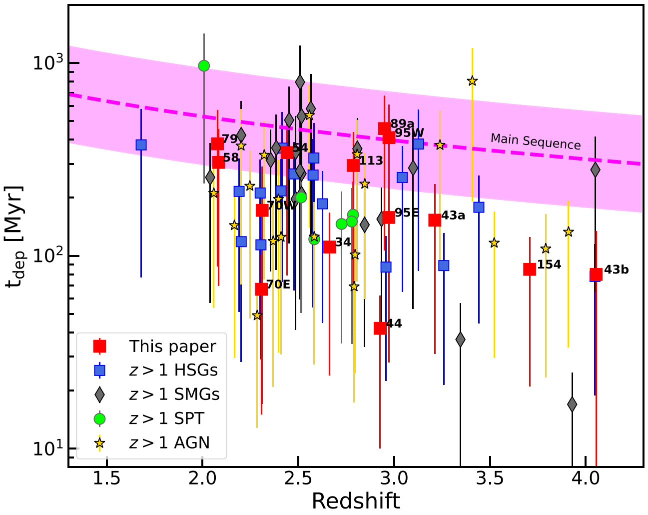

Figure 5. Depletion time ($t_{\rm dep}$) as a function of redshift. Our sample is plotted with red squares and the individual sources are labeled. We compare to sources from the literature, specifically the high-redshift DSFGs detected in CO(1−0) (see relevant references in Section 4.2). We estimate the $t_{\rm dep}$ of the literature sources making the same assumptions as for our sample, with an $\alpha_{\rm CO} = 3\ M_\odot$ (K km s^{-1} pc^2)$^{-1}$. However, the error bars plotted, include the range of $t_{\rm dep}$ that would be estimated using $\alpha_{\rm CO}$ from 0.8 to 4.3 $M_\odot$ (K km s^{-1} pc^2)$^{-1}$.

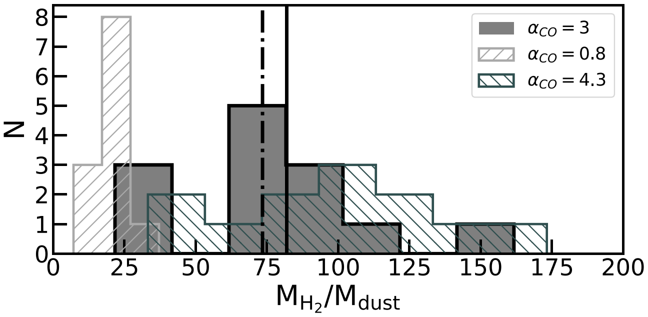

Figure 6. Histogram of the gas-to dust ratio ($M_{\rm gas}/M_{\rm dust}$) of our sample, for an $\alpha_{\rm CO} = 3\ M_\odot$ (K km s^{-1} pc^2)$^{-1}$, is plotted in solid. We also plot the histograms that result from assumptions of $\alpha_{\rm CO} = 0.8$ and 4.3 $M_\odot$ (K km s^{-1} pc^2)$^{-1}$ for comparison.

consequent $M_{\rm dust}$ estimates. Indeed in the study of Sharon et al. (2016) where the properties and line ratios of AGN and SMGs were compared, they found that although there is significant overlap between the two samples the lowest values were those of AGN.

In Figure 6 we also plot the distribution of the ratio when assuming $\alpha_{\rm CO} = 0.8$ and 4.3 with hollow histograms. An assumption of $\alpha_{\rm CO} = 0.8$ results in the whole sample having ratios below 40, while an $\alpha_{\rm CO} = 4.3$ does not change the distribution significantly.

4.4. CO Line Ratios and SLEDs

As our sample has been observed in multiple CO transitions in addition to CO(1−0), we can directly measure the CO brightness temperature ratios, r, by taking the ratio of the $L'_{\rm CO}$ of the different transitions over CO(1−0) (e.g., $r_{32/10} = L'_{\rm CO(3-2)}/L'_{\rm CO(1-0)}$). For HerBS-58, which only has the red component of the higher-J transitions detected in CO(1−0), we calculate an upper limit on the total flux and luminosity of the CO(1−0) line over the full line width observed for the higher-J lines and report the corresponding lower limit on the r values of this source. We find that the line ratios have a similar range of values across the different CO transitions, between 0.3 and 1.7 (see Table 5). In Figure 7 we plot the observed distributions for $r_{32/10} = L'_{\rm CO(3-2)}/L'_{\rm CO(1-0)}$, $r_{43/10} = L'_{\rm CO(4-3)}/L'_{\rm CO(1-0)}$, and $r_{54/10} = L'_{\rm CO(5-4)}/L'_{\rm CO(1-0)}$, with the typical range of values found for SMGs shown with a yellow filled region. Typical values of r for SMGs are $r_{32/10} = 0.4$–0.9, $r_{43/10} = 0.4$–0.7, $r_{54/10} = 0.4$–0.7, and $r_{65/10} = 0.2$–0.5 (e.g., Ivison et al. 2011; Bothwell et al. 2013; Spilker et al. 2014; Sharon et al. 2016; Harrington et al. 2021; Carilli & Walter 2013, and references therein). The majority of our samples have ratios consistent with the typical SMG values. However, it is interesting to note that the majority of the $r_{54/10}$ ratios are toward the higher end of the typical SMG values, although the small sample size limits the significance of this. HerBS-43b and HerBS-44 have

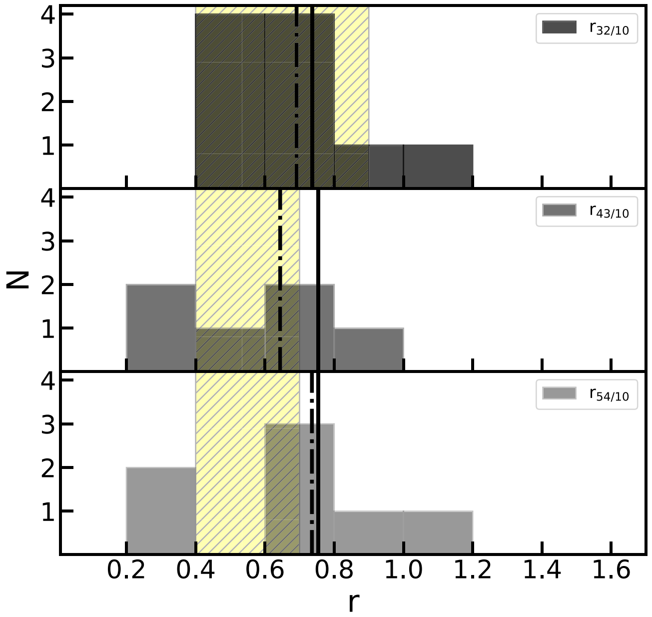

Figure 7. Histograms of the CO brightness temperature ratios, for different transitions: (top) $r_{32/10} = L'_{\rm CO(3-2)}/L'_{\rm CO(1-0)}$, (middle) $r_{43/10} = L'_{\rm CO(4-3)}/L'_{\rm CO(1-0)}$, (bottom) $r_{54/10} = L'_{\rm CO(5-4)}/L'_{\rm CO(1-0)}$. The solid line corresponds to the mean of the distribution, while the dotted–dashed corresponds to the median. The highlighted area corresponds to the range of average ratios found in the literature for the corresponding transitions.

Table 5
CO Brightness Temperature Ratios

Source	$r_{32/10}$	$r_{43/10}$	$r_{54/10}$	$r_{65/10}$
HerBS-34	0.7 ± 0.2	⋯	0.7 ± 0.2	⋯
HerBS-43a	⋯	0.9 ± 0.3	0.7 ± 0.2	⋯
HerBS-43b	⋯	1.7 ± 0.9	0.9 ± 0.5	(2.1 ± 1.1)
HerBS-44	1.4 ± 0.4	⋯	1.3 ± 0.3	⋯
HerBS-54	0.5 ± 0.1	0.6 ± 0.1	⋯	⋯
HerBS-58	>0.4	>0.2	⋯	⋯
HerBS-70E	0.6 ± 0.2	0.6 ± 0.2	⋯	⋯
HerBS-70W	1.1 ± 0.4	0.7 ± 0.2	⋯	⋯
HerBS-79	0.4 ± 0.1	0.3 ± 0.1	⋯	⋯
HerBS-89a	0.4 ± 0.1	⋯	0.31 ± 0.07	⋯
HerBS-95E	0.8 ± 0.2	⋯	1.0 ± 0.3	⋯
HerBS-95W	0.5 ± 0.1	⋯	0.3 ± 0.1	⋯
HerBS-113	0.9 ± 0.3	⋯	0.7 ± 0.2	⋯
HerBS-154	⋯	⋯	⋯	0.5 ± 0.1

ratios more in line with starburst-quasar systems such as APM08279+5255 (e.g., Riechers et al. 2009), but are still within the range of possible values for SMGs (see Sharon et al. 2016). We note that the $r_{65/10}$ of HerBS-43b is quite large, with a value that is nearly twice that of APM08279+5255; however, there is a large uncertainty on the CO(6−5) flux detected by Neri et al. (2020), which is reflected in the large error on this ratio.

In Figure 8, we plot the integrated CO fluxes of our sources, normalized to the CO(1−0). We have divided the sources into three different plots for easier comparison with the SLEDs of other DSFG samples from Bothwell et al. (2013) (32 SMGs at $1.2 < z < 4.1$), and Spilker et al. (2014) (22 SPT-selected SMGs at $2.0 < z < 5.7$), and the mean SLED of MS star-forming galaxies from Valentino et al. (2020). We also make a comparison with individual sources: Cosmic Eyelash (Danielson et al. 2011; Swinbank et al. 2011); GN20 (Carilli et al. 2010; Cortzen et al. 2020); the starburst-quasar galaxies Cloverleaf (Barvainis et al. 1997; Weiß et al. 2003; Bradford et al. 2009; Riechers et al. 2011b); APM08279+5255 (Papadopoulos et al. 2001; Riechers et al. 2006, 2009; Weiß et al. 2007); and M82 (Weiß et al. 2005). All SLEDs used for comparison are also normalized to the CO(1−0).

As can be seen in Figure 8, when comparing the normalized integrated flux values and respective curves, sources HerBS-54, HerBS-58, HerBS-79, HerBS-89a, and HerBS-95W are most comparable to other high-z SMGs, such as the Cosmic Eyelash, GN20, and the SMG sample of Bothwell et al. (2013). Sources HerBS-34, HerBS-43a, HerBS-70E, HerBS-70W, HerBS-113, and HerBS-154 are most comparable to the SPT SMGs of Spilker et al. (2014), the Cloverleaf galaxy, and the M82 center. Finally, sources HerBS-43b, HerBS-44, and HerBS-95E all lie between the two quasar-starburst systems Cloverleaf and APM08279+5255, which could indicate that these sources likely host an AGN. However, CO transitions at $J_{\rm up} > 6$ would be necessary to determine the presence of AGN excitation. Overall, the wide range of CO excitation we find for these sources demonstrates the importance of observing the CO(1−0) emission in galaxies when studying their molecular gas properties.

4.5. Radiative Transfer Modeling

Using the large velocity gradient statistical equilibrium method (e.g., Sobolev 1960), we modeled the molecular gas excitation conditions through the observed integrated fluxes of the multi-J CO lines. We adopt the one-dimensional (1D) non-LTE radiative transfer code `RADEX` (van der Tak et al. 2007), with an escape probability of $\beta = (1 - e^{-\tau})/\tau$ derived from an expanding sphere geometry. We used the CO collisional data from the LAMDA database (Schöier et al. 2005). With a Markov chain Monte Carlo approach following Yang et al. (2017), we explored the parameter space consisting of the kinetic temperature of the molecular gas ($T_{\rm K}$), the volume density ($n_{\rm H_2}$), the column density of CO per unit velocity gradient ($N_{\rm CO}/dV$), and the solid angle ($\Omega_{\rm app}$) of the source. The overall shape of the CO SLEDs only depends on $T_{\rm K}$, $n_{\rm H_2}$, and $N_{\rm CO}/dV$, and scales with $\Omega_{\rm app}$ (the magnification factors are also included in this factor). Therefore, we only focus on the parameters $T_{\rm K}$, $n_{\rm H_2}$, and $N_{\rm CO}/dV$ hereafter. As noted in the previous section, the CO(6−5) flux of HerBS-43b is quite uncertain and is an outlier when compared to the other transitions, therefore we chose to exclude it from our SLED modeling analysis. We note that a detailed analysis for the SLED of HerBS-89a was presented in Berta et al. (2021), where additional higher-J transitions were included. Here we present the analysis of the rest of the sample.

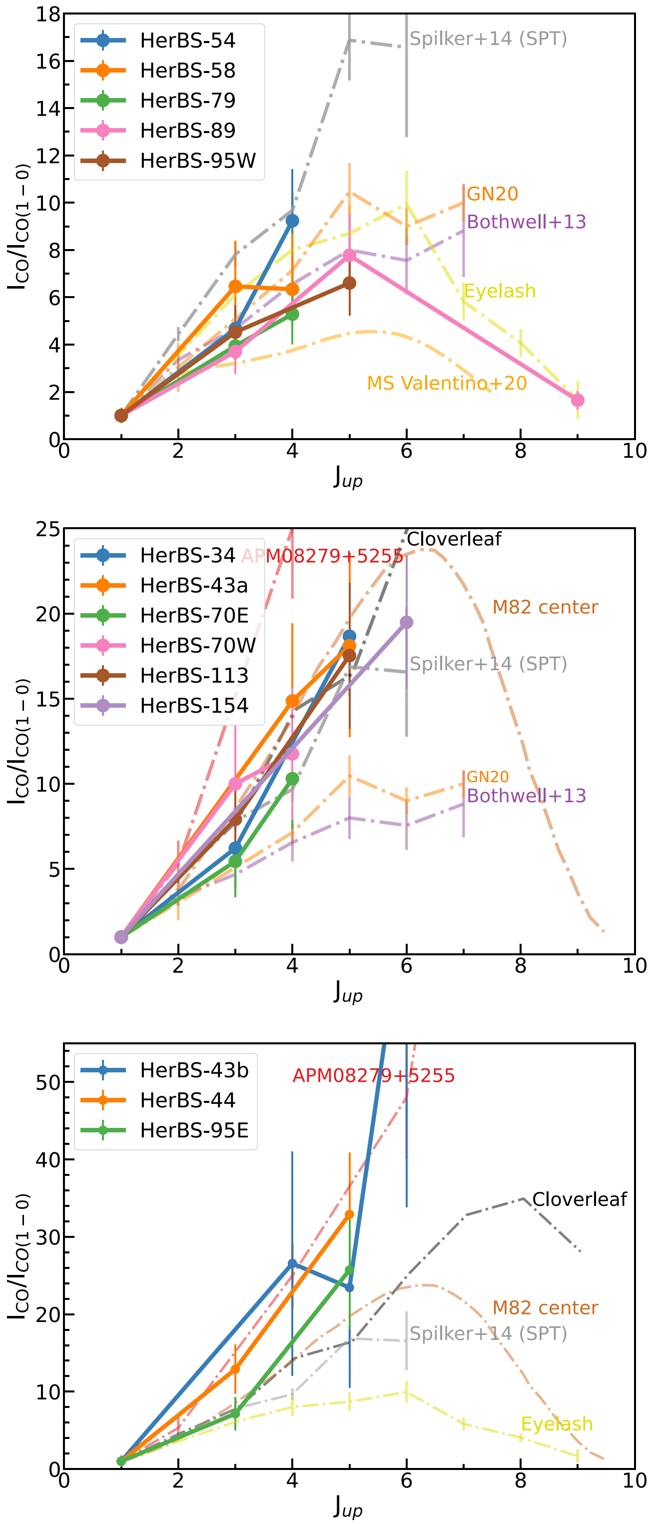

Figure 8. CO SLEDs, normalized to CO(1−0) for our sample. The sample has been split into three subsamples for easier distinction of the sources in the figures. The normalized integrated CO fluxes measured for each source are plotted as circles. For comparison we also plot SLEDs of other sources from the literature in dotted–dashed curves (see Section 4.5 for references). Note that for HerBS-89a we include the CO(9−8) transition and use the best-fit SLED model originally presented in Berta et al. (2021).

Table 6

Properties Derived from the Radiative Transfer Analysis, Where both the Median (Med) and the Maximum Likelihood (Max) Results for each Property Are Given (with the exception of $P_{\rm thermal}$)

Source	$\log(n_{\rm H2})$ ($\rm cm^{-3}$)		$\log(T_{\rm K})$ (K)		$\log(N_{\rm CO}/{\rm dV})$ ($\rm cm^{-2}\ km^{-1}\ s$)		$\log(P_{\rm thermal})$ ($\rm K\ cm^{-3}$)
	Med	Max	Med	Max	Med	Max	Med
HerBS-34	$3.69^{+0.95}_{-0.79}$	4.61	$2.06^{+0.42}_{-0.40}$	1.93	$18.09^{+0.28}_{-0.42}$	18.34	$5.80^{+0.71}_{-0.65}$
HerBS-43a	$2.97^{+0.66}_{-0.57}$	2.66	$2.22^{+0.49}_{-0.49}$	2.02	$17.58^{+0.52}_{-0.65}$	17.87	$5.29^{+0.45}_{-0.62}$
HerBS-43b	$3.92^{+0.73}_{-0.81}$	3.95	$2.24^{+0.39}_{-0.45}$	2.36	$17.82^{+0.47}_{-0.68}$	18.01	$6.19^{+0.54}_{-0.72}$
HerBS-44	$3.76^{+0.73}_{-0.59}$	3.84	$2.27^{+0.34}_{-0.41}$	2.33	$17.65^{+0.57}_{-0.53}$	17.91	$6.08^{+0.47}_{-0.43}$
HerBS-54	$3.18^{+1.00}_{-0.69}$	2.84	$2.09^{+0.44}_{-0.43}$	2.50	$17.89^{+0.41}_{-0.41}$	17.93	$5.32^{+0.75}_{-0.49}$
HerBS-58	$2.83^{+0.72}_{-0.51}$	2.96	$2.00^{+0.61}_{-0.62}$	1.81	$16.74^{+0.68}_{-0.72}$	16.68	$4.96^{+0.41}_{-0.48}$
HerBS-70E	$2.86^{+0.72}_{-0.52}$	3.38	$2.25^{+0.45}_{-0.44}$	2.39	$17.57^{+0.49}_{-0.60}$	17.37	$5.19^{+0.51}_{-0.52}$
HerBS-70W	$3.06^{+0.74}_{-0.57}$	3.35	$2.05^{+0.56}_{-0.51}$	1.88	$17.27^{+0.67}_{-0.85}$	16.55	$5.26^{+0.48}_{-0.68}$
HerBS-79	$2.49^{+0.42}_{-0.33}$	2.18	$2.29^{+0.45}_{-0.48}$	2.40	$16.89^{+0.42}_{-0.51}$	17.01	$4.82^{+0.36}_{-0.37}$
HerBS-95E	$3.93^{+0.66}_{-0.74}$	3.44	$2.25^{+0.33}_{-0.39}$	2.38	$18.03^{+0.33}_{-0.88}$	18.31	$6.19^{+0.56}_{-0.72}$
HerBS-95W	$2.55^{+0.66}_{-0.74}$	2.21	$2.31^{+0.44}_{-0.50}$	2.65	$17.21^{+0.35}_{-0.37}$	17.23	$4.93^{+0.34}_{-0.38}$
HerBS-113	$3.07^{+0.83}_{-0.63}$	2.62	$2.10^{+0.51}_{-0.43}$	2.51	$17.78^{+0.44}_{-0.53}$	17.66	$5.28^{+0.59}_{-0.57}$
HerBS-154	$3.09^{+0.63}_{-0.64}$	3.16	$2.24^{+0.48}_{-0.47}$	1.87	$17.51^{+0.57}_{-0.92}$	17.78	$5.44^{+0.41}_{-0.64}$

As most of the transitions of the CO lines observed are below $J_{\rm up} = 6$, there will be insufficient data to constrain the highly excited molecular gas component, assuming the HerBS galaxies are similar to those high-z SMGs, in which the CO excitation is dominated by two components peaking around $J_{\rm up} = 6$ and 8, respectively (Yang et al. 2017; Cañameras et al. 2018). To better constrain the posteriors, we have given slightly tighter boundaries for the flat priors of $n_{\rm H_2}$ and $N_{\rm CO}/dV$ than those used in Yang et al. (2017) (while other priors stay the same). Taking the values of the parameters from statistically studied SMG samples (Yang et al. 2017; Cañameras et al. 2018), we have chosen flat priors of $\log(n_{\rm H_2}/{\rm cm}^{-2}) = 2.0$–5.5 and $\log(N_{\rm CO}/dV/{\rm cm}^{-2}({\rm km/s})^{-1}) =$ 15.5–18.5. Similarly, we also limited the range of the thermal pressure $P_{\rm thermal}$ (defined by $P_{\rm thermal} = n_{\rm H_2} \times T_{\rm K}$) to be within 10^4 and 10^7 K cm^{-3}.

Two hundred walkers have been deployed with 500 iterations after the 100 burn-in ones. Thus, a total of 100,000 points of the solutions have been explored in parameter space.

The results of the radiative transfer analysis are reported in Table 6, indicating the $\pm 1\sigma$ values and the median of the posteriors. The maximum likelihood values are also listed in the table. The lack of measurements at $J_{\rm up} > 6$ for the majority of our sample means that the CO SLED models within $\pm 1\sigma$ of the best fit are significantly different at high J, leading to a relatively flat posterior of $T_{\rm K}$, and therefore a poor constraint on the maximum likelihood values (max). Therefore, we use the median (med) values to describe the fits. The CO data can be described with models of dense warm gas of $n_{\rm H_2} = 0.31 - 8.5 \times 10^3$ cm^{-3}, and $T_{\rm K} = 100$–200 K. These values are in general agreement with what has been found previously in high-z luminous DSFGs and SMGs (e.g., Combes et al. 2012; Danielson et al. 2013; Riechers et al. 2013; Spilker et al. 2014; Yang et al. 2017; Harrington et al. 2021).

A relation between $P_{\rm thermal}$ and SFE has been discussed in theoretical work (e.g., Elmegreen & Efremov 1997; Wong & Blitz 2002), suggesting that the main driver of the SFE in collapsing molecular clouds is the thermal gas pressure, or alternatively that higher pressures lead to more molecular clouds and a higher molecular gas fraction. Yang et al. (2017) examined whether there is evidence for this through the relationship between $P_{\rm thermal}$ and $L_{\rm IR}/L'_{\rm CO(1-0)}$ (as a proxy for SFE), in a sample of Herschel-selected luminous lensed DSFGs. A statistically significant correlation was found between $\log_{10}(P_{\rm thermal})$ and $\log_{10}(L_{\rm IR}/L'_{\rm CO(1-0)})$, spanning the range of environments from nearby galaxies to high-z luminous DSFGs, with no evidence of it being driven by the $n_{\rm H_2}$ or $T_{\rm K}$ values. Following Yang et al. (2017), in Figure 9 we plot the median values of $P_{\rm thermal}$ from the radiative transfer analysis as a function of $L_{\rm IR}/L'_{\rm CO(1-0)}$. In agreement with what was reported in Yang et al. (2017) we find that the data are following a correlation. We fit a line through the data in log space and find a strong correlation of $\log_{10}(P_{\rm thermal}) \propto 0.97 \times \log_{10}(L_{\rm IR}/L'_{\rm CO(1-0)})$, with the Pearson coefficient and p-value of 0.69 and 0.006, respectively. In addition, we color the data points based on the $\log_{10}(n_{\rm H_2})$ value, which allows us to simultaneously examine the presence of a dependence of $n_{\rm H_2}$ with $L_{\rm IR}/L'_{\rm CO(1-0)}$. We observe a trend in the $n_{\rm H_2}$ values showing an increase with higher $L_{\rm IR}/L'_{\rm CO(1-0)}$. To examine whether this positive trend of $n_{\rm H_2}$ values could be the driver of the observed correlation between $P_{\rm thermal}$ and $L_{\rm IR}/L'_{\rm CO(1-0)}$, we calculate the Pearson coefficient and p-value for a correlation between $n_{\rm H_2}$ and $L_{\rm IR}/L'_{\rm CO(1-0)}$. Indeed, we find evidence for a correlation of $n_{\rm H_2}$ with $L_{\rm IR}/L'_{\rm CO(1-0)}$, with a Pearson coefficient and p-value of 0.63 and 0.016, respectively. No evidence of a correlation between $T_{\rm K}$ and $L_{\rm IR}/L'_{\rm CO(1-0)}$ is found. This suggests that the $n_{\rm H_2}$ trend could be significantly contributing to the observed relation, but is not likely the driver as the correlation of $n_{\rm H_2}$ is less significant than that of $P_{\rm thermal}$. However, we remind the reader that our radiative transfer analysis is limited by the lack of CO transitions at $J > 6$.

5. Conclusions

In this paper, we have presented CO(1−0) observations using the VLA for 14 luminous DSFGs, including two binary systems, in the redshift range of $2 < z < 4$. These sources are part of the pilot project sample for the large NOEMA project z-GAL (P. Cox et al. 2023, in preparation), and were originally presented in Neri et al. (2020). Our main findings are the following:

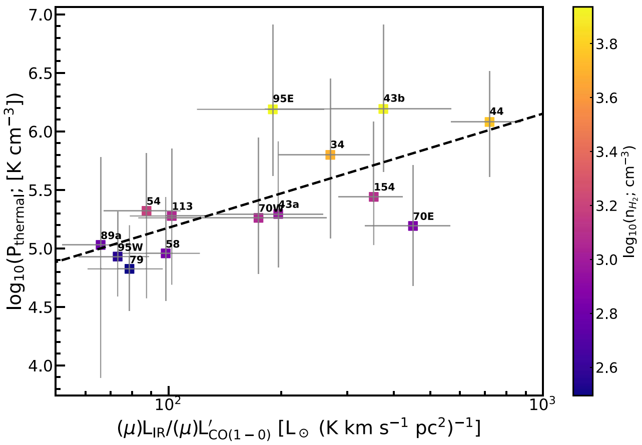

Figure 9. Median gas pressure ($P_{\rm thermal}$) from the median of the fitted models of the SLEDs, as a function of the $L_{\rm IR}/L'_{\rm CO(1-0)}$. The sources are plotted with a gradient color that corresponds to the median volume densities ($n_{\rm H_2}$).

1. We successfully detected the CO(1−0) emission in the entirety of our sample, resolving the molecular emission into extended and complex morphologies in half the sample (7/14 sources). For the majority of our sample, the CO(1−0) line profiles agree with those of the higher-J transitions.
2. Four of the sources were detected in the underlying radio continuum at observed frequencies of 20–38 GHz. Simple SED fitting to the far-IR and radio emission reveals that HerBS-43a, HerBS-43b, and HerBS-54 have radio emission consistent with their SFRs, while HerBS-70E has additional synchrotron radiation from an AGN.
3. We find that our sources have CO luminosities of $(\mu)L'_{\rm CO} = 0.4$–2.9×10^{11} K km s^{-1} pc^2. From these CO(1−0) luminosities, we estimated molecular gas masses of $(\mu)M_{\rm H_2} = 1.3$–$8.6 \times 10^{11}\ M_\odot$. By combining our CO(1−0) luminosities with the total IR (8–1000 μm) luminosities from Neri et al. (2020), we compare the molecular gas depletion times ($t_{\rm dep}$) and SFEs to other galaxy samples. We find that our sources have SFEs consistent with high-z DSFGs and low-z ULIRGs. Similarly, the depletion times of our sources cover a wide range and are consistent with both the MS and the starburst phase, with values of $t_{\rm dep} =$ 40–460 Myr.
4. We find a wide range of gas-to-dust ratios, $M_{\rm H_2}/M_{\rm dust} = 27$–167, in agreement with previous measurements for the majority of our sample. Three sources have surprisingly low ratios of <40, which could be a result of variation of $\alpha_{\rm CO}$ among the sample, or due to the presence of an AGN.
5. We find CO temperature brightness ratios of $r_{32/10} =$ 0.4–1.4, $r_{43/10} = 0.4$–1.7, and $r_{54/10} = 0.3$–1.3, with median values of 0.7, 0.6, and 0.7, respectively. The ratios are relatively consistent for the different transitions, with similar distributions. The range of values observed is in agreement with previous observations of high-z DSFGs and AGN (e.g., Sharon et al. 2016).
6. We find a wide range in the shapes of the CO SLEDs of our sample, highlighting the importance of CO(1−0) in revealing the range of excitation in such galaxies. We compare the SLEDs of our sources to those of the MS, typical SMGs, and starburst-quasar systems. The majority of our sample is consistent with high-z SMGs, with the exception of HerBS-43b, HerBS-44, and HerBS-95E, which are more comparable with the quasar-starburst systems, Cloverleaf, and APM08279+5255.
7. Finally, we perform radiative transfer modeling of the SLEDs following Yang et al. (2017). We find that our sample can be described with models of $n_{\rm H_2} =$ 0.3–8.5 $\times 10^3$ cm^{-3} and temperatures of $T_{\rm K} =$ 100–200 K. However, the results of the modeling are limited due to the lack of CO observations at the highest transitions. We examine the possible relation of the thermal gas pressure with SFE, by using the approximation of the $L_{\rm IR}/L'_{\rm CO(1-0)}$. We find strong evidence of a correlation, in agreement with the theoretical idea of thermal gas pressure having a direct role in the star formation process of these galaxies.

The results of this study emphasize the importance of anchoring the CO SLED to the ground state in order to determine the properties of the dense gas. Furthermore, by probing the underlying radio continuum we can trace the contribution to the radio emission from AGN and/or intense star formation in high-z DSFGs. Building on the previous studies of CO(1−0) in high-z DSFGs, our successful detection of the full sample with the high-angular resolution possible with the VLA, revealed a wide range of galaxy and excitation properties for a sample that would otherwise be classified as similarly luminous highly star-forming systems. The demonstrated success of this Pilot Study highlights the progress we will be able to achieve by measuring CO(1−0) in the full z-GAL sample of 126 Herschel-selected sources, in understanding the range of physical conditions that lead to the formation and evolution of luminous high-z DSFGs.

We thank the anonymous referee for their comments that helped improve the clarity of various aspects of the paper. This work is based on observations carried out under program VLA/20A-083 using the National Radio Astronomy Observatory's (NRAO) Karl G. Jansky Very Large Array. The National Radio Astronomy Observatory is a facility of the National Science Foundation operated under cooperative agreement by Associated Universities, Inc. This work benefited from the support of the project Z-GAL ANR-AAPG2019 of the French National Research Agency (ANR). B.M.J. acknowledges the support of a studentship grant from the UK Science and Technology Facilities Council (STFC) and funding from the Deutsche Forschungsgemeinschaft (DFG, German Research Foundation) Project SCHI 561/3-1. C.Y. acknowledges support from an ESO Fellowship. T.B. acknowledges funding from NAOJ ALMA Scientific Research Grant 2018-09B and JSPS KAKENHI No. 17H06130. H.D. acknowledges financial support from the Agencia Estatal de Investigación del Ministerio de Ciencia e Innovación (AEI-MCINN) under grant (La evolución de los cíumulos de galaxias desde el amanecer hasta el mediodía cósmico) with reference (PID2019-105776GB-I00/DOI:10.13039/501100011033) and acknowledge support from the ACIISI, Consejería de Economía, Conocimiento y Empleo del Gobierno de Canarias and the European Regional Development Fund (ERDF) under grant with reference PROID2020010107. S.J. acknowledges the financial support from the European Union's Horizon research and innovation program under the Marie Skłodowska-Curie grant agreement No. 101060888.

Appendix A
Individual Sources

In this appendix, we provide details of the CO(1−0) emission line profiles and the integrated-velocity maps for each source and compare them with the NOEMA 3 and 2 mm results described in Neri et al. (2020).

HerBS-34 is well detected in the CO(1−0) emission line displaying a profile that is comparable to the CO(3−2) line, although the ratio of CO(1−0) FWHM over the ΔV of higher-*J* transitions (FWHM/ΔV) is 1.8 ± 0.3. The large ratio is likely due to the lower S/N of the CO(1−0) line compared to the higher-*J* transitions. The CO emission remains fairly compact even when resolved, with an estimated size (deconvolved from the beam) of 1.″7 × 0.″9 (14 × 7 kpc).

HerBS-43a displays a similarly broad CO(1−0) emission line as the higher-*J* CO lines, with a ratio of FWHM/ΔV = 1.1 ± 0.2. The source is partially resolved, with an estimated size (deconvolved from the beam) of 1.″2 × 0.″9 (9 × 7 kpc).

HerBS-43b is the highest redshift source in our sample, and therefore has the weakest CO(1−0) emission line of the entire sample with a line flux of 0.064 ± 0.033 Jy kms^{-1}. The line profile of the CO(1−0) is nearly identical to that of the CO(4−3) line, showing the same double-peaked profile. The ratio of FWHM/ΔV = 0.9 ± 0.4. The source is partially resolved, with an estimated size (deconvolved from the beam) of 1.″1 × 0.″3 (8 × 2 kpc).

HerBS-44 has a strong CO(1−0) emission line with a single-peaked profile and an FWHM = 377 ± 64 km s^{-1} that is somewhat narrower than the high-*J* transitions, with a ratio of FWHM/ΔV = 0.7 ± 0.1. The source is elongated in the east–west direction with an estimated size (deconvolved from the beam) of 1.″1 × 0.″5 (9 × 4 kpc).

HerBS-54 has a very broad CO(1−0) line with FWHM = 1087 ± 176 km s^{-1} comparable to the high-*J* CO lines, with a ratio of FWHM/ΔV = 1.1 ± 0.3. With the new VLA observations, the source is resolved into a complex morphology showing two peaks within extended weaker emission. The peaks are separated by ∼1.″0 and the CO(1−0) emission extends over a region of ∼2.″2 (18 kpc).

HerBS-58 shows a complex morphology with two peaks along an arc-like feature to the west and a well-defined peak to the east. The overall extent of the CO emission is estimated to be 2.″1 × 1.″6 (18 × 14 kpc). The CO(1−0) line profile, which is best described by a single and relatively narrow Gaussian of FWHM = 363 ± 64 km s^{-1}, is redshifted at +300 km s^{-1} with respect to the center velocity corresponding to a $z_{\rm spec} = 2.0842$ as reported in Neri et al. (2020). The spectroscopic redshift for HerBS-58 was derived from the double-peaked [C I]($^3P_1-^3P_0$) emission line where both peaks have similar line fluxes. It is interesting to note that the CO(3−2) emission line shows a strong redshifted peak (at ∼300 km s^{-1}), corresponding to the CO(1−0) emission line, whereas the blueshifted component is at least 2× weaker. There is no clear evidence for a blueshifted CO component in the VLA data. A more detailed study of this source based on higher angular resolution NOEMA data will be presented in D. Ismael et al. 2023, (in preparation)

HerBS-70 is a binary system, which was originally resolved in Neri et al. (2020), including the sources HerBS-70E and HerBS-70W that are separated by 16.″5 corresponding to a projected distance of ∼140 kpc. Both are well detected and resolved in the CO(1−0) emission. HerBS-70E (to the east) has a wide emission line with FWHM = 622 ± 130 km s^{-1} comparable to the higher-*J* transitions, with a ratio of FWHM/ΔV = 0.8 ± 0.2. In contrast, *HerBS-70W* has a narrow line of FWHM = 197 ± 39 km s^{-1}, similar to the one seen in the higher-*J* CO lines with a ratio of FWHM/ΔV = 1.4 ± 0.3. Both sources display extended and somewhat resolved CO(1−0) emission with sizes of 1.″6 × 1.″2 (13 × 10 kpc), and 2.″1 × 1.″1 (18 × 9 kpc), for HerBS-70E and HerBS-70W, respectively.

HerBS-79 displays a broad CO(1−0) emission line with an FWHM = 787 ± 125 km s^{-1} that is comparable to the CO(3−2) and CO(4−3) profiles, with a ratio of FWHM/ΔV = 0.9 ± 0.2. The moment-0 map shows an extended arc-like morphology with a size of 2.″9 × 1.″0 (25 × 8 kpc) in the east–west direction.

The VLA data of HerBS-89a were originally published separately in Berta et al. (2021), a dedicated study of the source that combined the CO(1−0) observations with high-angular resolution NOEMA observations of the CO(9−8) emission line and additional emission or absorption lines of molecular tracers (including H_2O and OH^+). We have reanalyzed the CO(1−0) emission to be consistent with the analysis of the whole sample. We find a similar morphology and line profile as reported in Berta et al. (2021). However, the CO(1−0) from our extraction is slightly wider, with an FWHM = 1586 ± 244 km s^{-1} (versus 1433 ± 293 km s^{-1}) and the integrated line flux is significantly larger with $I_{\rm CO(1-0)}$ = 1.08 ± 0.22 Jy km s^{-1} (versus 0.64 ± 0.13 Jy km s^{-1}). The difference between the two results is due to the larger extraction region used in our analysis. The morphology of the CO(1−0) emission is arc-like, which was clearly resolved in the higher angular resolution NOEMA observations into a partial 1.″0 diameter Einstein ring in the dust emission and the molecular emission lines of CO(9−8) and $H_2O(2_{02}-1_{11})$. Based on a lensing model, the magnification of HerBS-89a was estimated to be $\mu \sim 5$ (see Berta et al. 2021).

HerBS-95 is the second binary system resolved by Neri et al. (2020), including the sources HerBS-95E and HerBS-95W, which are separated by 16.″4 corresponding to a projected distance of ∼130 kpc. HerBS-95E displays a CO(1−0) emission line that is somewhat blueshifted with respect to the expected rest-frame zero velocity, with a ratio of FWHM/ΔV = 0.8 ± 0.2. The emission is slightly extended with a size of 1.″5 × 0.″8 (12 × 6 kpc). HerBS-95W shows a double-peaked line profile with an FWHM = 522 km s^{-1}, in agreement with the higher-*J* transitions, with a ratio of FWHM/ΔV = 1.0 ± 0.2. The CO(1−0) emission has a centrally peaked but extended structure with a size of 2.″5 × 1.″9 (20 × 15 kpc).

HerBS-113 has a CO(1−0) profile somewhat narrower than the higher-*J* transitions with an FWHM = 497 km s^{-1}, with a ratio of FWHM/ΔV = 0.6 ± 0.2. The morphology of CO(1−0) emission is complex with three distinct peaks, distributed along an elongated ring-like structure and extending over ∼3″ (24 kpc). This morphology has been confirmed by higher resolution CO observations that will be presented in D. Ismail et al. (in preparation).

HerBS-154 displays a strong single-peaked CO(1−0) emission line with an FWHM = 384 ± 54 km s^{-1}, comparable to the higher-*J* CO and [C I]($^3P_1-^3P_0$) lines, with a ratio of FWHM/ΔV = 1.2 ± 0.2. The CO(1−0) emission has an extended arc-like morphology with a size of 2.″7 × 1.″7 (20 × 13 kpc).

Appendix B
Lensing

The large submillimeter surveys made with telescopes such as Herschel or SPT have revealed a significant population of bright high-redshift SMGs that are strongly gravitationally lensed, which become dominant for high flux densities ($S_{500\mu} > 100$ mJy) (e.g., Negrello et al. 2010; Mocanu et al. 2013; Wardlow et al. 2013). We therefore expect that some sources in our sample will be lensed, as discussed in Neri et al. (2020). The new CO(1−0) data have revealed that sources HerBS-54, HerBS-58, HerBS-79, HerBS-89a, HerBS-113, and HerBS-154 have complex morphologies such as arc-like structures, filaments, or multiple components, suggesting that these sources could be gravitationally lensed (see Figure 1). In the case of HerBS-89a higher resolution follow-up observations confirmed that it is indeed lensed (see Berta et al. 2021). However, for the rest of the sources, a derivation of the magnification based on the available data remains uncertain and deeper observations with higher angular resolution are needed to make a detailed lensing model.

In past studies, the relationship between $L'_{\mathrm{CO}(1-0)}$ and the FWHM of the CO(1−0) emission line has been discussed as a tool to estimate the magnification factor of high-redshift galaxies (e.g., Harris et al. 2012; Bothwell et al. 2013; Aravena et al. 2016; Neri et al. 2020). As $L'_{\mathrm{CO}(1-0)}$ is a measure of M_{H_2} and the CO(1−0) FWHM is related to the dynamical mass, this relationship is seen as a proxy to the Tully–Fisher relation (e.g., Isbell et al. 2018). Therefore, any sources lying above the expected correlation would be lensed. However, as shown in Aravena et al. (2016), the use of the $L'_{\mathrm{CO}(1-0)}$ versus FWHM relationship for measuring magnifications is highly unreliable, and can be typically off by factors of ∼2 or more.

In Figure 10, we plot $L'_{\mathrm{CO}(1-0)}$ as a function of the CO(1−0) FWHM for the sources of our sample together with sources previously observed in CO(1−0). We limit our comparison to high-redshift sources that are unlensed and sources for which the gravitational magnification has been reliably estimated based on lensing model analysis. Therefore, we remove uncertainties that can accompany conversions from higher-J CO transitions or sources that were defined as magnified using this same relation. The known lensed sources (identified in the figure) were not corrected for magnification. The dotted line shows the best-fitting relationship from Bothwell et al. (2013) and the dashed line represents the derived parameterization for L'_{CO} by Bothwell et al. (2013) for a disk galaxy, that can be described as

$$L'_{\mathrm{CO}} = C\left(\frac{\Delta V}{2.35}\right)^2 \frac{R}{\alpha\, G}, \tag{B1}$$

where ΔV is the FWHM of the CO in kilometers per second, $R = 7$ kpc is the radius of the CO emitting region in parsecs, G is gravitational constant, α is the CO luminosity to gas mass conversion factor, and $C = 2.1$ is the constant parameterizing the galaxy's disk morphology.

We use the compilation of CO(1−0) detected galaxies and fit all sources that are unlensed and the lensed sources after correcting for magnification, as well as only those at $z > 1$. Both relationships show a less steep correlation than previously found. We note that we plot the lensed sources without the magnification correction, even though we correct them for magnification for the fit, in order to better visualize the parameter space covered by the lensed sources, in relation to the unlensed sources and the relations.

Overall, we find a large scatter for both the lensed and unlensed galaxies, consistent with what has been reported in previous studies (e.g., Aravena et al. 2016). Sources with magnifications of <10 mostly cover a similar region of the parameter space as the unlensed sources, with only highly lensed galaxies ($\mu > 10$) showing clear offsets. This strengthens the conclusions of Aravena et al. (2016) on the unreliability of this relation as a precise measure of magnification (see also the discussions in, e.g., Dannerbauer et al. 2017; Aravena et al. 2019; Jin et al. 2021). It is interesting to note the specific example of HerBS-89a, which is based on the $L'_{\mathrm{CO}(1-0)}$–FWHM relationship would be considered to be an unlensed source when compared to the Bothwell et al. (2013) relation, and therefore an HyLIRG (see Neri et al. 2020), was found to be lensed with a magnification of ∼5 based on high-angular resolution observations and a lensing model (Berta et al. 2021). For the above reasons, we do not attempt to determine the magnifications of our sample using this method.

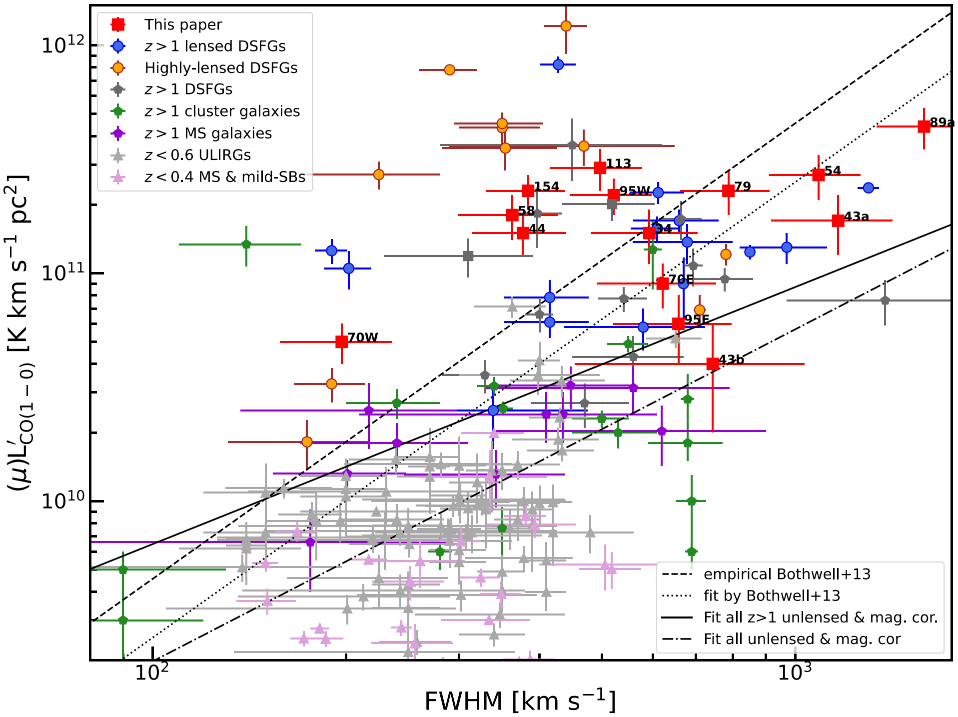

Figure 10. $L'_{\rm CO(1-0)}$ vs. the FWHM of the CO(1−0) emission line. The sample of sources presented in this paper are shown with large red squares (and identified by their name), and are compared to other high-z lensed and unlensed luminous DSFGs (Ivison et al. 2011; Harris et al. 2012; Carilli & Walter 2013; Aravena et al. 2016; Bakx et al. 2020b, and references therein), $z > 1$ MS galaxies (Aravena et al. 2014) and cluster galaxies (Rudnick et al. 2017; Wang et al. 2018), as well as low-z ULIRGs, mild-starburst (mild-SBs) and MS galaxies (Solomon et al. 1997; Chung et al. 2009; Combes et al. 2011; Geach et al. 2011; Villanueva et al. 2017). Only sources with reported CO(1−0) emission lines have been included to avoid uncertainties in estimating $L'_{\rm CO(1-0)}$ from higher-J transitions. No correction for magnification was applied to the CO luminosities. Sources with magnifications >10 are classified as highly lensed SMGs. The dotted and dashed lines represent the relationships described in Bothwell et al. (2013) (see the text and Equation (B1)); the solid and dashed–dotted lines display fits to all the $z > 1$ galaxies and the entire sample of sources, respectively, that are unlensed and have been corrected for magnification.

ORCID iDs

F. Stanley https://orcid.org/0000-0003-2156-8386
B. M. Jones https://orcid.org/0000-0002-0675-0078
D. A. Riechers https://orcid.org/0000-0001-9585-1462
C. Yang https://orcid.org/0000-0002-8117-9991
S. Berta https://orcid.org/0000-0002-0320-1532
P. Cox https://orcid.org/0000-0003-2027-8221
T. J. L. C. Bakx https://orcid.org/0000-0002-5268-2221
H. Dannerbauer https://orcid.org/0000-0001-7147-3575
S. Dye https://orcid.org/0000-0002-1318-8343
R. J. Ivison https://orcid.org/0000-0001-5118-1313
S. Jin https://orcid.org/0000-0002-8412-7951
M. Lehnert https://orcid.org/0000-0003-1939-5885
R. Neri https://orcid.org/0000-0002-7176-4046
A. Omont https://orcid.org/0000-0002-4721-3922
P. van der Werf https://orcid.org/0000-0001-5434-5942
A. Weiss https://orcid.org/0000-0003-4678-3939

References

Aravena, M., Decarli, R., Gónzalez-López, J., et al. 2019, ApJ, 882, 136
Aravena, M., Hodge, J. A., Wagg, J., et al. 2014, MNRAS, 442, 558
Aravena, M., Murphy, E. J., Aguirre, J. E., et al. 2013, MNRAS, 433, 498
Aravena, M., Spilker, J. S., Bethermin, M., et al. 2016, MNRAS, 457, 4406
Bakx, T. J. L. C., Eales, S., & Amvrosiadis, A. 2020a, MNRAS, 493, 4276
Bakx, T. J. L. C., Eales, S. A., Negrello, M., et al. 2018, MNRAS, 473, 1751
Bakx, T. J. L. C., Dannerbauer, H., Frayer, D., et al. 2020b, MNRAS, 496, 2372
Barvainis, R., Maloney, P., Antonucci, R., & Alloin, D. 1997, ApJ, 484, 695
Becker, R. H., White, R. L., & Helfand, D. J. 1995, ApJ, 450, 559
Berta, S., Young, A. J., Cox, P., et al. 2021, A&A, 646, A122
Blain, A. W., Smail, I., Ivison, R. J., Kneib, J. P., & Frayer, D. T. 2002, PhR, 369, 111
Bolatto, A. D., Wolfire, M., & Leroy, A. K. 2013, ARA&A, 51, 207
Bothwell, M. S., Smail, I., Chapman, S. C., et al. 2013, MNRAS, 429, 3047
Bourne, N., Dunlop, J. S., Merlin, E., et al. 2017, MNRAS, 467, 1360
Bouwens, R., González-López, J., Aravena, M., et al. 2020, ApJ, 902, 112
Bouwens, R. J., Aravena, M., Decarli, R., et al. 2016, ApJ, 833, 72
Bradford, C. M., Aguirre, J. E., Aikin, R., et al. 2009, ApJ, 705, 112
Bussmann, R. S., Pérez-Fournon, I., Amber, S., et al. 2013, ApJ, 779, 25
Bussmann, R. S., Riechers, D., Fialkov, A., et al. 2015, ApJ, 812, 43
Cañameras, R., Nesvadba, N. P. H., Guery, D., et al. 2015, A&A, 581, A105
Cañameras, R., Yang, C., Nesvadba, N. P. H., et al. 2018, A&A, 620, A61
Carilli, C. L., Daddi, E., Riechers, D., et al. 2010, ApJ, 714, 1407
Carilli, C. L., & Walter, F. 2013, ARA&A, 51, 105
Carlstrom, J. E., Ade, P. A. R., Aird, K. A., et al. 2011, PASP, 123, 568
Casey, C. M., Narayanan, D., & Cooray, A. 2014, PhR, 541, 45
Chabrier, G. 2003, PASP, 115, 763
Chung, A., Narayanan, G., Yun, M. S., Heyer, M., & Erickson, N. R. 2009, AJ, 138, 858
Combes, F., García-Burillo, S., Braine, J., et al. 2011, A&A, 528, A124
Combes, F., Rex, M., Rawle, T. D., et al. 2012, A&A, 538, L4
Condon, J. J. 1992, ARA&A, 30, 575
Conley, A., Cooray, A., Vieira, J. D., et al. 2011, ApJL, 732, L35
Cortzen, I., Magdis, G. E., Valentino, F., et al. 2020, A&A, 634, L14
Cox, P., Krips, M., Neri, R., et al. 2011, ApJ, 740, 63
da Cunha, E., Groves, B., Walter, F., et al. 2013, ApJ, 766, 13
Danielson, A. L. R., Swinbank, A. M., Smail, I., et al. 2011, MNRAS, 410, 1687
Danielson, A. L. R., Swinbank, A. M., Smail, I., et al. 2013, MNRAS, 436, 2793
Danielson, A. L. R., Swinbank, A. M., Smail, I., et al. 2017, ApJ, 840, 78
Dannerbauer, H., Harrington, K., Díaz-Sánchez, A., et al. 2019, AJ, 158, 34
Dannerbauer, H., Lehnert, M. D., Emonts, B., et al. 2017, A&A, 608, A48
Delhaize, J., Smolčić, V., Delvecchio, I., et al. 2017, A&A, 602, A4
Downes, D., & Solomon, P. M. 1998, ApJ, 507, 615
Draine, B. T., & Li, A. 2007, ApJ, 657, 810

Dunne, L., Maddox, S. J., Papadopoulos, P. P., Ivison, R. J., & Gomez, H. L. 2022, MNRAS, 517, 962
Dunne, L., Maddox, S. J., Vlahakis, C., & Gomez, H. L. 2021, MNRAS, 501, 2573
Dye, S., Eales, S. A., Gomez, H. L., et al. 2022, MNRAS, 510, 3734
Eales, S., Dunne, L., Clements, D., et al. 2010, PASP, 122, 499
Elmegreen, B. G., & Efremov, Y. N. 1997, ApJ, 480, 235
Fu, H., Cooray, A., Feruglio, C., et al. 2013, Natur, 498, 338
Fudamoto, Y., Ivison, R. J., Oteo, I., et al. 2017, MNRAS, 472, 2028
Geach, J. E., Smail, I., Moran, S. M., et al. 2011, ApJL, 730, L19
Genzel, R., Tacconi, L. J., Gracia-Carpio, J., et al. 2010, MNRAS, 407, 2091
Genzel, R., Tacconi, L. J., Lutz, D., et al. 2015, ApJ, 800, 20
George, R. D., Ivison, R. J., Hopwood, R., et al. 2013, MNRAS, 436, L99
Gómez-Guijarro, C., Riechers, D. A., Pavesi, R., et al. 2019, ApJ, 872, 117
Hardcastle, M. J., Gürkan, G., van Weeren, R. J., et al. 2016, MNRAS, 462, 1910
Harrington, K. C., Weiss, A., Yun, M. S., et al. 2021, ApJ, 908, 95
Harris, A. I., Baker, A. J., Frayer, D. T., et al. 2012, ApJ, 752, 152
Harris, A. I., Baker, A. J., Zonak, S. G., et al. 2010, ApJ, 723, 1139
Hatsukade, B., Kohno, K., Yamaguchi, Y., et al. 2018, PASJ, 70, 105
Hodge, J. A., & da Cunha, E. 2020, RSOS, 7, 200556
Isbell, J. W., Xue, R., & Fu, H. 2018, ApJL, 869, L37
Ivison, R. J., Page, M. J., Cirasuolo, M., et al. 2019, MNRAS, 489, 427
Ivison, R. J., Papadopoulos, P. P., Smail, I., et al. 2011, MNRAS, 412, 1913
Ivison, R. J., Swinbank, A. M., Smail, I., et al. 2013, ApJ, 772, 137
Jin, S., Dannerbauer, H., Emonts, B., et al. 2021, A&A, 652, A11
Kennicutt, R. C., Jr. 1989, ApJ, 344, 685
Lestrade, J.-F., Carilli, C. L., Thanjavur, K., et al. 2011, ApJL, 739, L30
Lupu, R. E., Scott, K. S., Aguirre, J. E., et al. 2012, ApJ, 757, 135
Madau, P., & Dickinson, M. 2014, ARA&A, 52, 415
Maddox, S. J., Valiante, E., Cigan, P., et al. 2018, ApJS, 236, 30
Magnelli, B., Ivison, R. J., Lutz, D., et al. 2015, A&A, 573, A45
Magnelli, B., Popesso, P., Berta, S., et al. 2013, A&A, 553, A132
McMullin, J. P., Waters, B., Schiebel, D., Young, W., & Golap, K. 2007, in ASP Conf. Ser. 376, Astronomical Data Analysis Software and Systems XVI, ed. R. A. Shaw, F. Hill, & D. J. Bell (San Francisco, CA: ASP), 127
Mocanu, L. M., Crawford, T. M., Vieira, J. D., et al. 2013, ApJ, 779, 61
Nayyeri, H., Keele, M., Cooray, A., et al. 2016, ApJ, 823, 17
Negrello, M., Amber, S., Amvrosiadis, A., et al. 2017, MNRAS, 465, 3558
Negrello, M., Hopwood, R., De Zotti, G., et al. 2010, Sci, 330, 800
Neri, R., Cox, P., Omont, A., et al. 2020, A&A, 635, A7
Oliver, S. J., Bock, J., Altieri, B., et al. 2012, MNRAS, 424, 1614
Oteo, I., Ivison, R. J., Dunne, L., et al. 2016, ApJ, 827, 34
Oteo, I., Ivison, R. J., Dunne, L., et al. 2018, ApJ, 856, 72
Papadopoulos, P., Ivison, R., Carilli, C., & Lewis, G. 2001, Natur, 409, 58
Penney, J. I., Blain, A. W., Assef, R. J., et al. 2020, MNRAS, 496, 1565
Pilbratt, G. L., Riedinger, J. R., Passvogel, T., et al. 2010, A&A, 518, L1
Planck Collaboration, Aghanim, N., Akrami, Y., et al. 2020, A&A, 641, A6
Planck Collaboration, Aghanim, N., Altieri, B., et al. 2015, A&A, 582, A30
Reuter, C., Vieira, J. D., Spilker, J. S., et al. 2020, ApJ, 902, 78
Riechers, D. A., Bradford, C. M., Clements, D. L., et al. 2013, Natur, 496, 329
Riechers, D. A., Carilli, C. L., Maddalena, R. J., et al. 2011b, ApJL, 739, L32
Riechers, D. A., Carilli, L. C., Walter, F., et al. 2011a, ApJL, 733, L11
Riechers, D. A., Cooray, A., Omont, A., et al. 2011c, ApJL, 733, L12
Riechers, D. A., Hodge, J., Walter, F., Carilli, C. L., & Bertoldi, F. 2011d, ApJL, 739, L31
Riechers, D. A., Leung, T. K. D., Ivison, R. J., et al. 2017, ApJ, 850, 1
Riechers, D. A., Walter, F., Carilli, C. L., & Lewis, G. F. 2009, ApJ, 690, 463
Riechers, D. A., Walter, F., Carilli, C. L., et al. 2006, ApJ, 650, 604
Rudnick, G., Hodge, J., Walter, F., et al. 2017, ApJ, 849, 27
Sandstrom, K. M., Leroy, A. K., Walter, F., et al. 2013, ApJ, 777, 5
Schöier, F. L., van der Tak, F. F. S., van Dishoeck, E. F., & Black, J. H. 2005, A&A, 432, 369
Sharon, C. E., Riechers, D. A., Hodge, J., et al. 2016, ApJ, 827, 18
Sobolev, V. V. 1960, Moving Envelopes of Stars (Cambridge, MA: Harvard Univ. Press)
Solomon, P. M., Downes, D., Radford, S. J. E., & Barrett, J. W. 1997, ApJ, 478, 144
Spilker, J. S., Marrone, D. P., Aguirre, J. E., et al. 2014, ApJ, 785, 149
Strandet, M. L., Weiss, A., Vieira, J. D., et al. 2016, ApJ, 822, 80
Swinbank, A. M., Papadopoulos, P. P., Cox, P., et al. 2011, ApJ, 742, 11
Tacconi, L. J., Genzel, R., Saintonge, A., et al. 2018, ApJ, 853, 179
Tacconi, L. J., Genzel, R., Smail, I., et al. 2008, ApJ, 680, 246
Tacconi, L. J., Genzel, R., & Sternberg, A. 2020, ARA&A, 58, 157
Tacconi, L. J., Neri, R., Genzel, R., et al. 2013, ApJ, 768, 74
Thomson, A. P., Ivison, R. J., Simpson, J. M., et al. 2014, MNRAS, 442, 577
Thomson, A. P., Ivison, R. J., Smail, I., et al. 2012, MNRAS, 425, 2203
Urquhart, S. A., Bendo, G. J., Serjeant, S., et al. 2022, MNRAS, 511, 3017
Valentino, F., Daddi, E., Puglisi, A., et al. 2020, A&A, 641, A155
Valiante, E., Smith, M. W. L., Eales, S., et al. 2016, MNRAS, 462, 3146
van der Tak, F. F. S., Black, J. H., Schöier, F. L., Jansen, D. J., & van Dishoeck, E. F. 2007, A&A, 468, 627
Vieira, J. D., Crawford, T. M., Switzer, E. R., et al. 2010, ApJ, 719, 763
Vieira, J. D., Marrone, D. P., Chapman, S. C., et al. 2013, Natur, 495, 344
Viero, M. P., Asboth, V., Roseboom, I. G., et al. 2014, ApJS, 210, 22
Villanueva, V., Ibar, E., Hughes, T. M., et al. 2017, MNRAS, 470, 3775
Walter, F., Decarli, R., Carilli, C., et al. 2012, Natur, 486, 233
Wang, T., Elbaz, D., Daddi, E., et al. 2018, ApJL, 867, L29
Wardlow, J. L., Cooray, A., De Bernardis, F., et al. 2013, ApJ, 762, 59
Weiß, A., De Breuck, C., Marrone, D. P., et al. 2013, ApJ, 767, 88
Weiß, A., Downes, D., Neri, R., et al. 2007, A&A, 467, 955
Weiß, A., Henkel, C., Downes, D., & Walter, F. 2003, A&A, 409, L41
Weiß, A., Ivison, R. J., Downes, D., et al. 2009, ApJL, 705, L45
Weiß, A., Walter, F., & Scoville, N. Z. 2005, A&A, 438, 533
Wong, T., & Blitz, L. 2002, ApJ, 569, 157
Yang, C., Omont, A., Beelen, A., et al. 2017, A&A, 608, A144
Zavala, J. A., Casey, C. M., Manning, S. M., et al. 2021, ApJ, 909, 165